

Polarised radio filaments outside the Galactic plane

Matias Vidal^{*}, C. Dickinson, R. D. Davies and J. P. Leahy

Jodrell Bank Centre for Astrophysics, Alan Turing Building, School of Physics and Astronomy, The University of Manchester, Oxford Road, Manchester M13 9PL, UK.

15 June 2015

ABSTRACT

We used data from the *WMAP* satellite at 23, 33 and 41 GHz to study the diffuse polarised emission over the entire sky. The emission originates mostly from filamentary structures with well-ordered magnetic fields. Some of these structures have been known for decades in radio continuum maps. Their origin is not clear and there are many filaments that are visible for the first time. We have identified and studied 11 filaments. The polarisation fraction of some of them can be as high as 40%, which is a signature of a well ordered magnetic field. The polarisation spectral indices, averaged over 18 regions in the sky is $\beta = -3.06 \pm 0.02$, consistent with synchrotron radiation. There are significant variations in β over the sky ($\Delta\beta \approx 0.2$).

We explore the link between the large-scale filaments and the local ISM, using the model of an expanding shell in the solar vicinity. We compared observed polarisation angles with the predictions from the model and found good agreement. This strongly suggests that many large scale filaments and loops are nearby structures. This is important in the context of the Galactic magnetic field as these structures are normally included in global models, neglecting the fact that they might be local. We also studied the level of contamination added by the diffuse filaments to the CMB polarisation power spectra. We conclude that, even though these filaments present low radio brightness, a careful removal will be necessary for future all-sky CMB polarisation analysis.

Key words: diffuse radiation – polarisation – radio continuum: ISM – ISM: magnetic fields – radiation mechanism: general – radiation mechanism: non-thermal

1 INTRODUCTION

The “radio loops” are some of the largest structures on the sky and have been studied for more than 50 years. Some of these structures, are also visible in microwaves, X-rays and gamma-rays. [Brown, Davies & Hazard \(1960\)](#) review for the first time possible theories about the origin of the most obvious of them, Loop I, also called the North Polar Spur (NPS). Loop II ([Large, Quigley & Haslam 1962](#)), Loop III ([Quigley & Haslam 1965](#)) and Loop IV ([Large, Quigley & Haslam 1966](#)) were discovered shortly after. The emission from all these features is non-thermal with temperature spectral indices ($T_b \propto \nu^\beta$) β around 1 GHz ranging between -2.7 and -2.9 ([Berkhuijsen 1973](#); [Borka 2007](#)). These loops are also visible in polarisation, both in starlight ([Mathewson & Ford 1970](#)) and radio ([Page et al. 2007](#)).

There are different interpretations for the origin of these loops and their true nature is not completely clear. The lack of precise measurements of their distance is the main limitation in their study. Four possible explanations for their origin have been proposed:

- Old and nearby supernova remnants ([Berkhuijsen, Haslam & Salter 1971](#); [Spoelstra 1973](#))
- Outflow from the Galactic Centre ([Sofue 1977](#); [Bland-Hawthorn & Cohen 2003](#))
- Bubbles/shells powered by OB associations ([Egger 1995](#); [Wolleben 2007](#)).
- Magnetic field loops illuminated by relativistic electrons ([Heiles 1998](#)).

The spectral indices of these structures indicate a synchrotron origin for the radio emission. At frequencies below ~ 1 GHz, synchrotron dominates the sky brightness. The synchrotron intensity depends on the relativistic electron density (n_e), their energy distributions and the strength of the magnetic field. The energy distribution of cosmic ray electrons (CRE) is observed to follow a power-law, $N(E) \propto E^{-p}$ for energies $E > 10$ GeV (e.g. [Adriani et al. 2011](#); [Ackermann et al. 2012](#)). Gamma-ray data suggests that this distribution is fairly smooth, both spectrally and spatially over the sky ([Strong, Moskalenko & Reimer 2004](#); [Strong, Moskalenko & Ptuskin 2007](#)). Typical values measured for the spectral index p are close to $p = 3$, and therefore, this value is usually adopted in synchrotron and magnetic field modelling (e.g. [Miville-Deschênes et al. 2008](#); [Jaffe et al. 2010](#)).

^{*} E-mail: matias.vidal@manchester.ac.uk (MV)

Synchrotron emission is intrinsically linearly polarised. For a uniform magnetic field, the fractional polarisation is $\Pi = (p + 1)/(p + 7/3)$. For a typical value of cosmic ray spectral index ($p \approx 3$) the polarisation fraction can be as high as 75%. The observed value is smaller than this due to superposition of different field directions along the line-of-sight, beam averaging and, at cm-wavelengths, intrinsic Faraday rotation.

The synchrotron spectral index can vary spatially across the sky (e.g. [Lawson et al. 1987](#); [Reich & Reich 1988](#)) and also with frequency (see e.g. [Banday & Wolfendale 1991](#); [Giardino et al. 2002](#); [Platania et al. 2003](#)). The loss of energy of the CRE through synchrotron radiation is larger at higher energies ($\propto E^2$), so over time, the synchrotron spectral index becomes steeper (more negative). β is also expected to be steeper with higher Galactic latitude ([Strong, Moskalenko & Ptuskin 2007](#)). This is because most cosmic rays are produced in supernova (SN) explosions, close to the Galactic plane. As the CRE diffuse away from the plane, to higher Galactic latitudes, the ageing effect will produce a steepening in the synchrotron spectral index.

Averaged values for the measured spectral indices vary from $\beta = -2.55$ between 45 MHz and 408 MHz ([Guzmán et al. 2011](#)), $\beta = -2.71$ between 408 MHz and 2.3 GHz ([Platania et al. 2003](#); [Giardino et al. 2002](#)) and $\beta = -3.01$ between 23 GHz and 33 GHz ([Davies et al. 2006](#); [Dunkley et al. 2009](#); [Dickinson et al. 2009](#)). [Macellari et al. \(2011\)](#) measured the synchrotron spectral index over the entire sky using polarisation and intensity data from *WMAP* between 23 and 33 GHz, and found it to be $\beta = -3.32 \pm 0.12$ for intensity and $\beta = -3.01 \pm 0.03$ for polarised intensity. More recently [Fuskeland et al. \(2014\)](#) have measured small variations in the synchrotron polarisation spectral index using *WMAP* polarisation data at 23 and 33 GHz.

In this paper we aim to characterise the filamentary structure visible in the polarised sky of *WMAP*. The relatively high frequency of the *WMAP* bands is useful to study the polarised Galactic synchrotron because Faraday rotation is negligible at this frequency range. This allows us to study the emission from regions on the Galactic plane in the inner Galaxy, which are washed out by Faraday rotation in low-frequency polarisation surveys.

The paper is organised as follows: Section 2 describes the data and the processing applied to it, such as smoothing and bias correction. In Section 3 we define a number of filaments that are visible in polarised intensity and measure how close the observed magnetic field vectors are to the orientation of the filament. A spectral index analysis in polarisation is described in Section 4 while in Section 5 we study the polarisation fraction at K-band. In Section 7 we discuss the different results and Section 8 gives conclusions.

2 DATA PROCESSING

2.1 WMAP data

In this work, we use the 9-year *WMAP* maps ([Bennett et al. 2013](#)) available from the Legacy Archive for Microwave Background Data Analysis (LAMBDA) website¹. The data consist of 5 full sky maps of the Stokes I , Q and U parameters at central frequencies of 22.7 GHz (K-band), 32.9 GHz (Ka-band), 40.6 GHz (Q-band), 60.5 GHz (V-band) and 93.0 GHz (W-band) with the corresponding beam profiles and noise models. We focus on K, Ka and Q-bands where the signal-to-noise ratio (SNR) is highest and syn-

chrotron can be detected at least along bright filaments. Besides, dust contamination at these frequencies is negligible. The maps are provided in the HEALPix² pixelisation scheme ([Górski et al. 2005](#)) with $N_{\text{side}} = 512$, which corresponds to a pixel size of $\sim 7'$.

2.2 Smoothing

To increase the SNR of the maps, and to minimise any systematic effect due to beam-asymmetries in polarisation, we smoothed the maps to common resolutions of 1° and 3° full-width-half-maximum (FWHM). The filaments that we study are typically diffuse at scales larger than 1° . The smoothing was done by first deconvolving in harmonic space the azimuthally symmetrized effective beam and then convolving with a Gaussian beam. [Wehus, Fuskeland & Eriksen \(2013\)](#) showed that the beam asymmetries in *WMAP* K- and Ka-bands give rise to unstable spectral index measurements in polarisation. Here we will use an effective resolution of 3° for measuring the spectral indices so the beam asymmetries have minimal impact. We also generated smoothed maps with an angular resolution of 1° FWHM to study the polarisation angle direction along the filamentary structures. After smoothing, the 3° resolution maps were downgraded to a HEALPix resolution of $N_{\text{side}} = 32$ (pixel size $\sim 1.8^\circ$) while the 1° resolution maps were downgraded to $N_{\text{side}} = 256$ (pixel size $\sim 13.6'$).

In order to assess the noise level after the smoothing of the maps, we ran Monte Carlo simulations to calculate the uncertainties after the smoothing and pixel downgrading. We generated 500 normally distributed noise realisations of Stokes I , Q and U for each frequency band based on the covariance matrix from the *WMAP* data. We calculated the statistics of this assembly and we used the dispersion on each pixel (for the I , Q , and U maps) as the statistical error on the 3° smoothed maps. We also calculated the covariance term between Q and U for the ensemble (σ_{QU}^2). By this route, we have smoothed maps for Stokes I , Q and U with their respective uncertainties and (Q, U) correlations for each pixel. We note that this is an underestimate of the uncertainty due to the presence of correlated noise in large scales. For all the noise values estimated, we need to add in quadrature the 0.2% *WMAP* absolute calibration error ([Bennett et al. 2013](#)).

2.3 Polarisation bias

It has long been known that observations of linear polarisation are subject to bias ([Serkowski 1958](#)). Given the positive nature of $P = \sqrt{Q^2 + U^2}$, even if the true Stokes parameters are zero, P will yield a positive estimate in the presence of noise. The effect is particularly important in the low SNR regime.

Ways to correct for the bias have been studied in detail ([Wardle & Kronberg 1974](#); [Simmons & Stewart 1985](#); [Vaillancourt 2006](#); [Quinn 2012](#)) for the special case where the uncertainties for (Q, U) are equal and normally distributed around their true value (Q_0, U_0). [Wardle & Kronberg \(1974\)](#) proposed an estimator, which is widely used both for its simplicity and for its good performance. The debiased polarisation intensity, P_{wk} , is calculated as

$$P_{wk} = \sqrt{P' - \sigma_P^2}, \quad (1)$$

where $P' = \sqrt{Q^2 + U^2}$ is the observed linear polarisation intensity and $\sigma_P = \sigma_Q = \sigma_U$.

¹ <http://lambda.gsfc.nasa.gov>

² <http://healpix.sourceforge.net/>

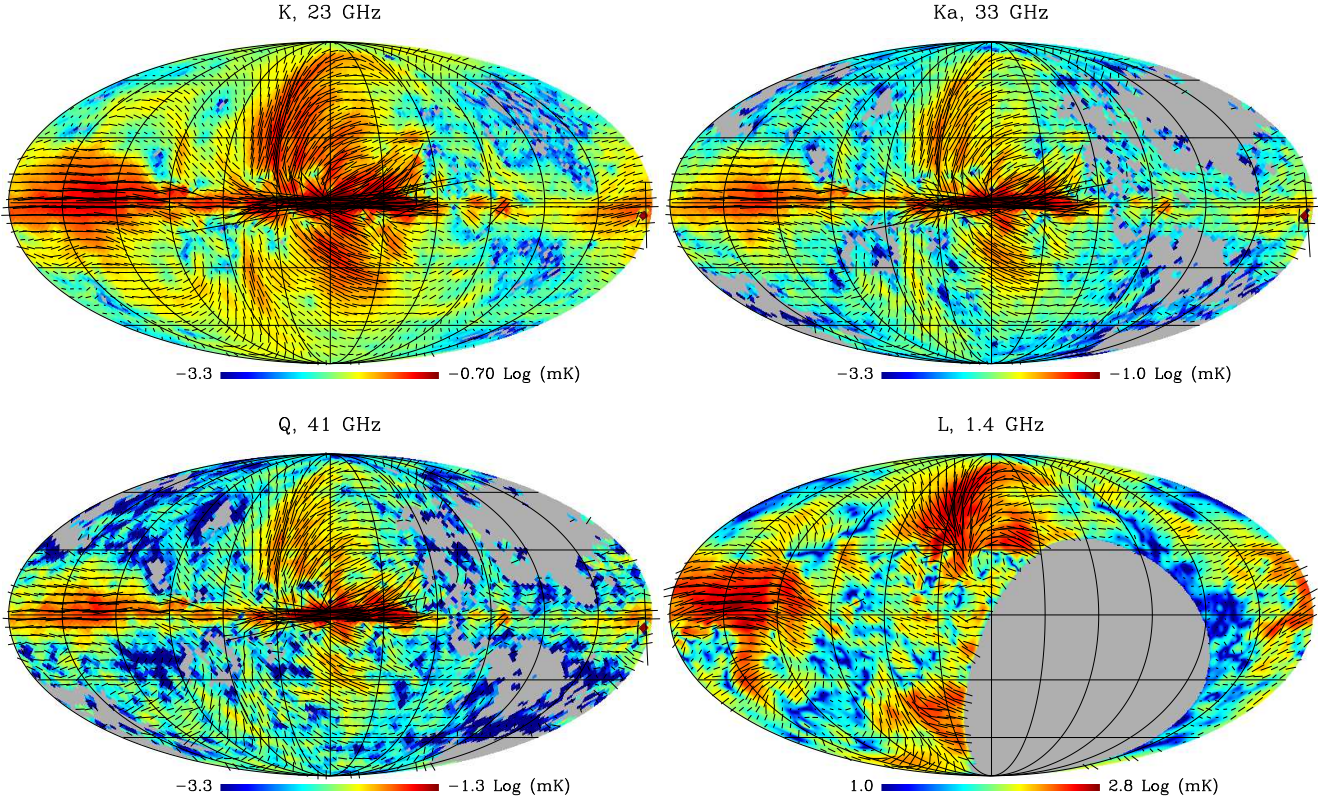


Figure 1. Polarisation intensity maps of *WMAP* K- (top left), Ka- (top right) and Q-band (bottom left) and the Wolleben et al. (2006) 1.4 GHz map (bottom right). The vectors indicate the magnetic field direction and their length is proportional to the polarisation intensity. All maps have been smoothed to an angular resolution of 3° FWHM. The *WMAP* maps have been corrected for polarisation bias. The masked areas (grey pixels) in the Ka and Q-band maps correspond to the regions where the SNR in the polarisation angle at K-band is lower than 5. The masked area in the 1.4 GHz map is the region that was not observed during the survey. The Galactic coordinate grid has a separation of $30^\circ \times 30^\circ$.

The case with asymmetric uncertainties ($\sigma_Q \neq \sigma_U$) on the other hand is interesting as many polarisation data sets have this characteristic. In particular, the correlations between the (Q, U) uncertainties in *WMAP* data are mainly due to non-uniform azimuthal coverage for each pixel in the sky. In this case, the bias will depend on the polarisation angle χ as well as on p . A generalisation of the Wardle & Kronberg estimator can be written for this case. It has the form:

$$\hat{p}_{wk} = \sqrt{P^2 - (\sigma_Q^2 \sin^2 2\chi' + \sigma_U^2 \cos^2 2\chi' - 2\sigma_{QU} \cos 2\chi' \sin 2\chi')}, \quad (2)$$

where σ_{QU} is the correlation term of the uncertainty in Q, U . This estimator reduces to Eq. 1 when the errors are isotropic. Here, the observed polarisation angle, χ' is used as a surrogate for the true polarisation angle χ . At the high SNR regime (e.g. the bright regions in *WMAP* K-band), the approximation $\chi' \approx \chi$ is excellent. For instance, for a SNR of 15, the uncertainty in the polarisation angle $\sigma_\chi \approx 1^\circ.9$.

The estimator in Eq. 2 can be used to de-bias the polarisation maps at K-band, where there is a reasonable SNR ($\gtrsim 5\sigma$) along large areas of the sky. For the rest of the bands, where the SNR is lower we can derive a new estimator. For this, we use the fact that we can obtain a good estimation of the *true* polarisation angle χ from *WMAP* K-band. Moreover, at *WMAP* frequencies, Faraday rotation is negligible over most of the sky (see Section 6) so we can assume that the polarisation angle χ observed at K-band, will be the same at the higher frequency bands. The additional infor-

mation about the polarisation angle in the higher frequency bands will help to reduce the total bias in the pixels with low SNR. The new estimator requires the observed Q', U' values, the uncertainties $\sigma_Q, \sigma_U, \sigma_{QU}$ and an independent measurement of the polarisation angle χ . The derivation for this known-angle estimator and the test of its performances is described in Vidal, Leahy & Dickinson (2014). The estimator takes the following form:

$$\hat{p}_\chi = \frac{\sigma_U^2 Q' \cos 2\chi - \sigma_{QU} (Q' \sin 2\chi + U' \cos 2\chi) + \sigma_Q^2 U' \sin 2\chi}{\sigma_U^2 \cos^2 2\chi - 2\sigma_{QU} \sin 2\chi \cos 2\chi + \sigma_Q^2 \sin^2 2\chi}. \quad (3)$$

and its uncertainty,

$$\sigma_{\hat{p}_\chi}^2 = \frac{\sigma_Q^2 \sigma_U^2 - \sigma_{QU}^2}{\sigma_U^2 \cos^2 2\chi - 2\sigma_{QU} \sin 2\chi \cos 2\chi + \sigma_Q^2 \sin^2 2\chi}. \quad (4)$$

In Vidal, Leahy & Dickinson (2014), simulations are used to test the effectiveness of this new estimator and to quantify any residual bias due to noise in χ .

In summary, we use the generalised Wardle & Kronberg estimator from Eq. 2 to correct the polarisation intensity map at K-band and the known-angle estimator to correct the Ka and Q-band maps.

2.4 Bias-corrected polarisation maps

We prepared bias-corrected polarisation intensity maps of *WMAP* K, Ka and Q-bands maps, smoothed to a common resolution of 3° . At K-band, some pixels show a noise value (terms inside the bracket in Eq. 2) that is larger than the observed polarisation intensity. This will produce some pixels with imaginary values after the bias correction (see Eq. 2). These pixels are masked-out for the analysis. Given the nature of the known-angle de-biasing method that we use for Ka- and Q-bands –the knowledge of the true polarisation angle– we have masked out the pixels that show an uncertainty in the polarisation angle at K-band larger than $5^\circ 8$, which are the ones that have a SNR in polarisation intensity, $\text{SNR}_p < 5$. This corresponds to a total masked sky-area of 17.3%. This SNR cutoff was chosen to be sure that any residual bias will be smaller than 5%, as shown in Vidal, Leahy & Dickinson (2014). In Fig. 1 we show the maps, with the masked areas shown as grey. Also plotted on each map are the polarisation vectors, aligned parallel to the magnetic field direction (we have rotated the vectors by 90°). We also include the 1.4 GHz polarisation map from Wolleben et al. (2006).

By looking at *WMAP* K-band in Fig. 1, it can be seen that most of the emission outside the Galactic plane comes from a number of individual large scale features. Regions we can easily identify are the Galactic plane, the fan region centred at $l \approx 140^\circ$, and a number of loops and filaments that run mostly perpendicular to the Galactic plane. The biggest of these filaments is Loop I, running perpendicular to the plane at $l \sim 30^\circ$. We note also that the magnetic field vectors are coherent with the direction of the filamentary structures; we will quantify this observation in the next section.

The most obvious difference between the *WMAP* maps and the Wolleben map at 1.4 GHz is the inner Galaxy between $b \lesssim |30^\circ|$. Faraday rotation produces a depolarisation region in the 1.4 GHz map, which cancels out most of the polarised emission close to the Galactic plane, but as noted above, this is negligible at *WMAP* frequencies, except towards the Galactic Centre (see Section 6).

3 POLARISED LARGE-SCALE FEATURES.

A number of radio loops have been described in the literature, Loop I or NPS being the best known. Most have been observed in low frequency ($\nu < 1$ GHz) continuum radio surveys. Six loops have been described in the literature. These loops are well fitted by small circles on the sky (see e.g. Berkhuijsen, Haslam & Salter 1971) in the low frequency continuum data. Table 1 lists some properties of the loops along with comments and references. We identify the loops in polarisation based on the 1° de-biased polarised intensity map at K-band. Additionally, we prepared a high-pass filtered version of the 0.408 GHz map from Haslam et al. (1982) to highlight the filamentary structure in the continuum map. This was done using an unsharp-mask (Sofue, Reich & Reich 1989) which filters out the emission at angular scales larger than 10° . In Fig. 2 we show the *WMAP* K-band polarisation intensity map and the filtered version of the 0.408 GHz Haslam et al. map.

A number of filaments are easily recognisable over the sky; most of them lie in the inner Galaxy, with Galactic longitude in the range $-90^\circ < l < 90^\circ$. Here we concentrate on the filaments that have a “circular” arc shape. The continuum loops I, III and IV are visible in polarisation although the more diffuse Loop II is not obvious.

We fitted small-circle arcs to the coordinates of the pixels that

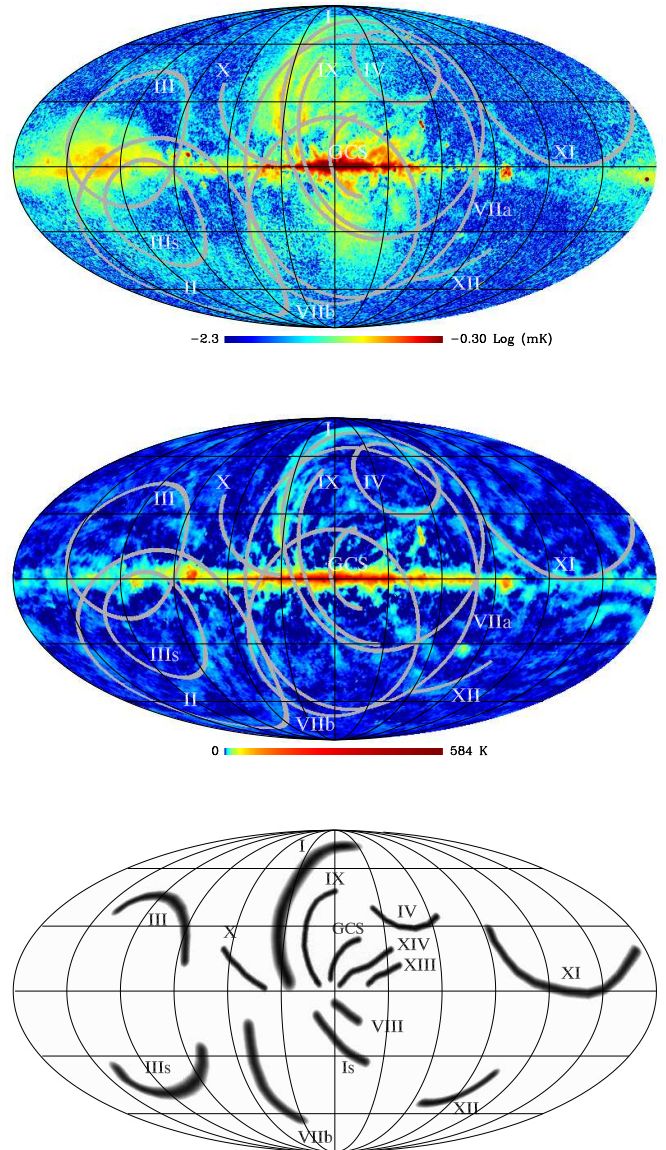


Figure 2. *Top:* *WMAP* K-band polarisation intensity map. *Middle:* Unsharp mask version of the Haslam et al. map. The angular resolution of the unfiltered maps is 1° and the filter beam has a size of 10° FWHM. The location and sizes of the 13 loops and arcs are listed in Table 1. *Bottom:* Template showing the filaments visible on the *top* panel. They are defined following maximum brightness points along each filament.

trace the peak of the circular features in Fig. 2. Table 1 lists the parameters found for the three previously known continuum loops that are visible in the polarisation data, as well as the parameters published on the literature from continuum fits to the data. We did not attempt to fit for Loop II (Cetus Arc) due to the very low emission observed in the *WMAP* polarisation maps. There is a good agreement for the radii and centres of the loops between the low frequency continuum data and the *WMAP* polarisation data. Loop III is the one that shows the larger discrepancy between the geometry measured in continuum with respect to polarisation, where the emission in polarisation peaks 5° away from the continuum. This

Table 1. Circular loops and filaments parameters. The *top* section lists the previously identified continuum loops. The *middle* section lists the loops and circular arcs that are visible only in polarisation. The *bottom* section lists the filaments that are not circular arcs. The 14 loops, arcs and filaments that are visible in polarisation are shown in the *bottom* panel of Fig. 2. All the numerical values in the table are in degrees.

Loop Name	Continuum			Polarisation			Comments / Reference
	l	b	r	l	b	r	
I	329.0	17.5	58	332.6	20.7	54.3	NPS, Brown, Davies & Hazard (1960)
II	100.0	−32.5	45.5	---	---	---	Large, Quigley & Haslam (1962)
III	124.0	15.5	32.5	118.8	13.2	31.6	Quigley & Haslam (1965)
IV	315.0	48.5	19.8	315.8	48.1	19.3	Large, Quigley & Haslam (1966)
V	127.5	18.0	67.2	---	---	---	Milogradov-Turin & Urošević (1997), same as loop III.
VI	120.5	30.8	72.4	---	---	---	Milogradov-Turin & Urošević (1997), not visible in <i>WMAP</i> polarisation.
GCS	---	---	---	344.0	4.8	18.5	Galactic centre spur from Sofue, Reich & Reich (1989).
III [*]	---	---	---	106	−22	50.0	Below the plane at the “fan” region.
VIIa	---	---	---	345.0	0.0	65	From Wolleben (2007) using the 1.4 GHz map.
VIIb [*]	---	---	---	0.7	−23.3	45.9	Values found in this work for VIIa.
IX [*]	---	---	---	332.0	16	46.5	Inside the NPS.
X [*]	---	---	---	30	35	67.0	Tangential to the plane.
XI [*]	---	---	---	227	38	81.0	Large arc tangential to the plane.
XII	---	---	---	300	0.7	27.6	Close to the LMC.
VIII	---	---	---	---	---	---	Southern part of the GCS?
XIII	---	---	---	---	---	---	Weak continuum emission at 0.408 GHz.
XIV	---	---	---	---	---	---	Possible HI counterpart (see Sec. 7.1). Weak continuum emission at 0.408 GHz.

*: These arcs are clearly visible only in polarisation.

shift between the total intensity and the polarisation morphology was previously noted by Spoelstra (1972).

We have identified five new arcs that are visible only in these polarisation data (marked with an asterisk in Table 1) that can be fitted by small circle arcs. Wolleben (2007) identifies a “New Loop” (loop VIIa in our nomenclature) using the 1.4 GHz polarisation map from the DRAO survey (Wolleben et al. 2006). The 1.4 GHz maps present a depolarisation band at Galactic latitudes $|b| < 30^\circ$ due to Faraday depolarisation. Because of this, they only use data at $b < -35^\circ$ to define the location and size of this new loop. Here we include data closer to the Galactic plane that belongs to the arc in order to define its geometry. This filament is brighter closer to the Galactic plane and is listed as VIIb.

3.1 Polarisation angle along filaments

The direction of the ordered component of the magnetic field can give us information about the origin of the observed filaments. The magnetic fields of old SN (e.g. the DA 530 supernova; Landecker et al. 1999) are tangential to the surface of the shell. This is traditionally explained by the compression of the field in radiative shocks with large radius (see e.g. the review by Reynolds, Gaensler & Bocchino 2012).

Looking at the de-biased *WMAP* K-band polarisation map from Fig. 1, we see that most of the emission at high latitudes comes from individual filamentary structures. We also can see that the magnetic field direction vectors are roughly parallel to the direction of the filaments. We will quantify this observation by comparing the polarisation angle χ with the direction of the filament.

In the *top* panel of Fig. 2, there are some features that are not well fitted by a circular arc. We include some of these non-circular features in this analysis, and also ignore some of the loops and arcs that are listed in Table 1 due to their low surface brightness. The filaments that we use in this analysis are shown in Fig. 2.

In order to define the direction α of the filaments that we want to compare with the polarisation angle χ , we connected pairwise the points of maximum brightness across each filament shown in the *top* panel of Fig. 2 using great circle arcs. This created a map with a smooth line that follows the direction of each filament. Then, this maximum brightness template for each filament was convolved with a Gaussian beam of a width similar to the apparent width of the filament, typically $2^\circ - 4^\circ$. In the *bottom* panel of Fig. 2 we can see the resulting templates for all the filaments that we study here.

The direction at each point of the filament, α , can be calculated using the spatial gradient of the previously described template map for the filaments, T . The gradient of this map points to a direction that is perpendicular to the extension of the filament, so that we will have,

$$\alpha = \arctan \left(\frac{\partial T / \partial \theta}{\partial T / \partial \phi / \sin \theta} \right), \quad (5)$$

where θ and ϕ are the spherical coordinates. The $\sin(\theta)$ factor appears because of the use of spherical coordinates.

α defines the direction of steepest gradient moving away from the filament axis, so $\alpha \pm 90$ defines the orientation of the filament axis, defined in the same sense as the position angle of polarization.

We measured the difference between the observed polarisation angle $\chi = 0.5 \arctan(U/Q)$ and the direction angle α . We did this in adjacent circular apertures along each filament, with a diameter between 3° and 5° depending on the size of the filament. Figs. 3, 4 and 5 show maps of each filament with the circular apertures where we calculate the angle difference. A thick black line in the maps indicates the direction of the filament defined from the template map and the gradient method described. Also are plotted, for each filament, the difference between the observed polarisation angle and the angle of the filament. The error bars incorporate both the random fluctuations given by the dispersion of the measured angles in each aperture and an additional 5° systematic uncertainty added to

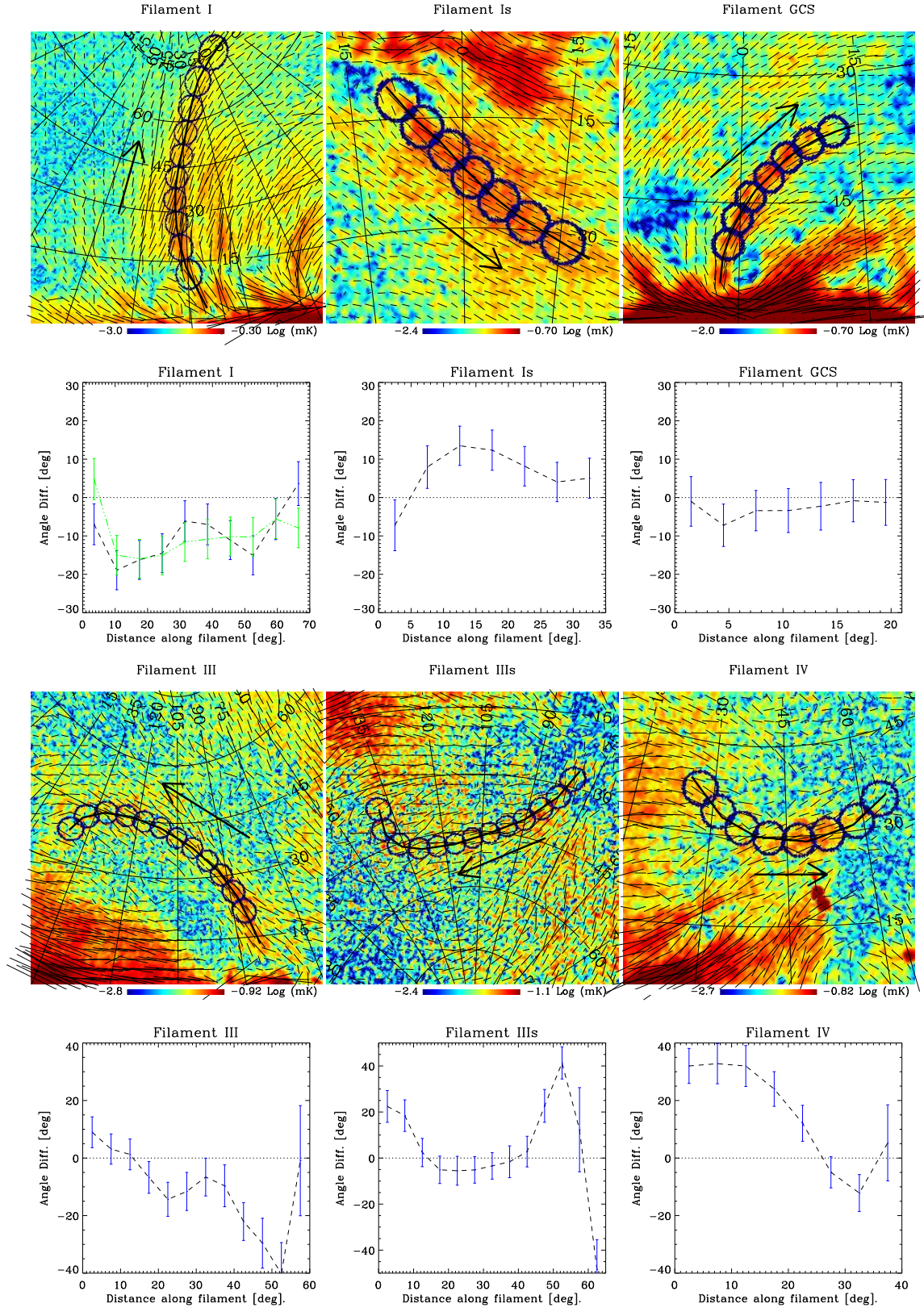


Figure 3. The panels on the *top* show maps of each filament as defined in the *bottom* panel of Fig 2. The adjacent circles in each filament show the apertures that we use to measure the difference between the polarisation angle (represented by the small black vectors) and the direction of the filament (defined by thin grey line running along the filament). The panels at the *bottom* show the difference between the polarisation angle, χ , and the angle defined by the direction of each filament, α , along the filament. In these plots, the distance along the filament is measured in the direction indicated by the black arrow. The error bars represent the random fluctuation in the polarisation angle, including an additional 5° uncertainty assigned as a conservative systematic error in the definition of the direction of the filament.

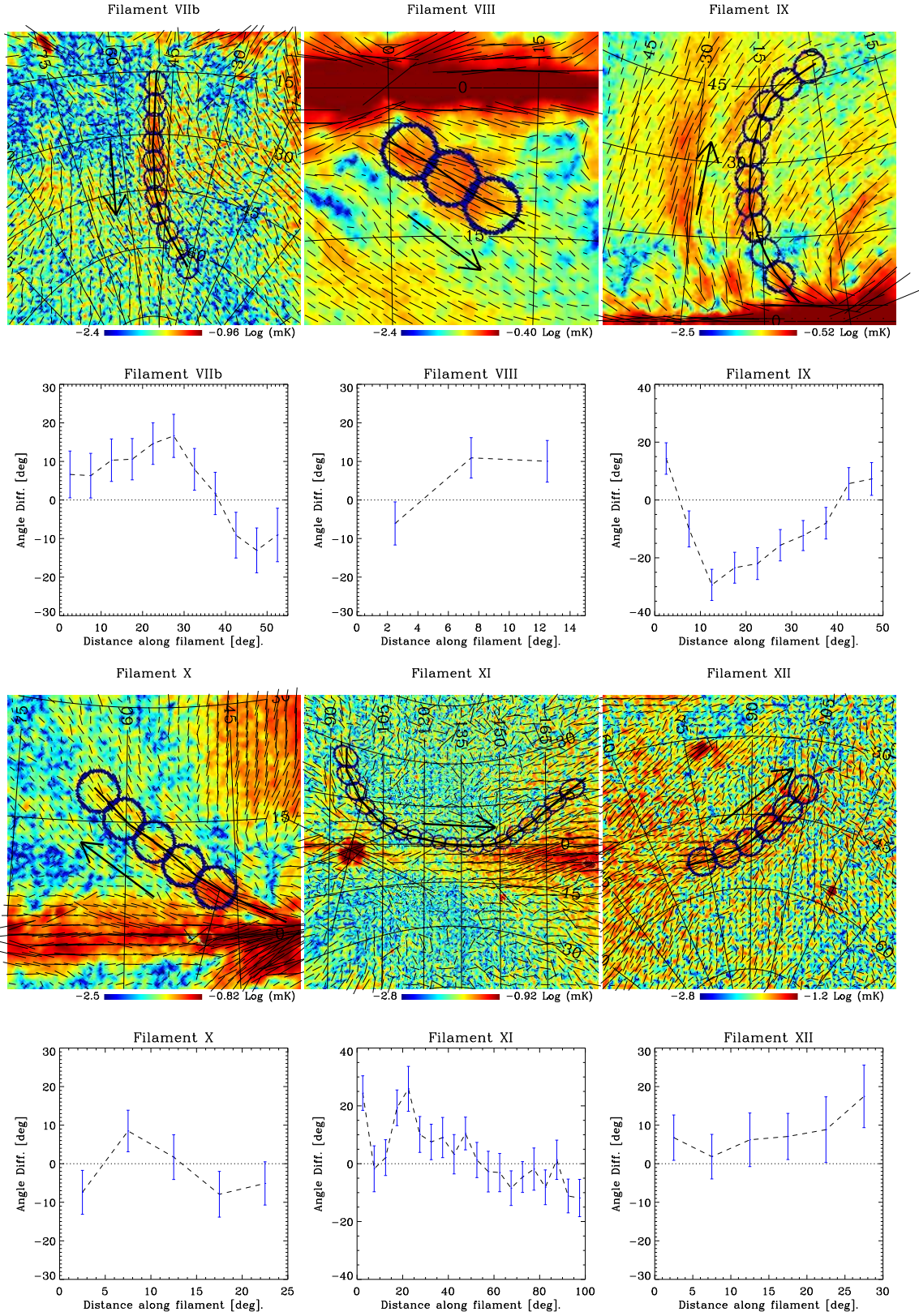


Figure 4. Continuation of Figure 3

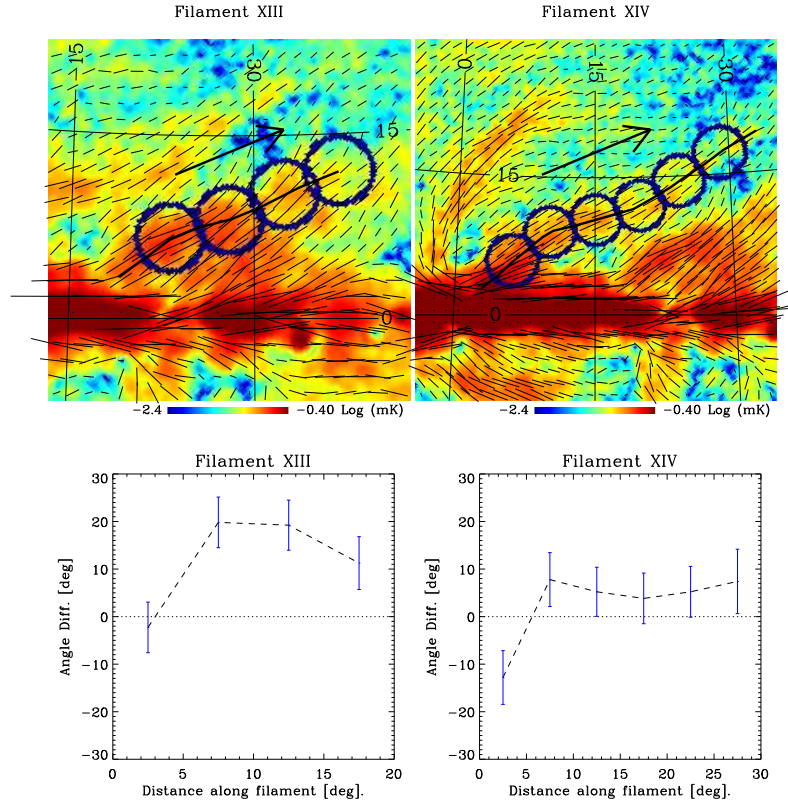


Figure 5. Continuation of Figure 3

account for small errors in the definition of the spatial direction of each filament.

For the NPS (Filament I in our numbering), we also compared the polarisation angle χ with the direction angle defined by the geometry of the loop in total intensity, i.e. the circular fit that traditionally is used to describe the NPS, listed in Table 1. The green line in that figure represents the angle that the circular loop defines. The difference between the circular loop and our definition for the direction of the NPS using the gradient technique is small compared with the uncertainties, so there is consistency between the two definitions for the direction of the filament.

In the Galactic Centre Spur (GCS), the difference in angle is small, averaging less than 5° . The magnetic field vectors are very close to parallel with the direction of the filament. In Filament No. I, the NPS, there is an offset of $\sim 10^\circ$ in the angles. It can be seen even by looking at the map on Fig. 3. A similar difference occurs in Filament IX. Filament X is also well-aligned, with a difference very close to zero within the errors. Filaments III, IIIs, VIIb, XI and XII are those with less signal-to-noise ratio, and the polarisation angle on them is not parallel to their extension, there are even inversions in the sign of the difference of the angles. Filaments Is and VIII also have a systematic difference in angles but in this case, the difference is positive. Emission from Filament XIV is well aligned along its extension. Finally, Filament XIII shows a systematic positive difference of $\sim 15^\circ$.

It is interesting that in the inner Galaxy, the deviations from parallel in the direction of the angles are different on the north Galactic hemisphere compared with the south (compare filaments I and IX in the north with Filaments Is and VIII in the south). The direction of the emission from these filaments has a smaller radius

of curvature than the one defined by the polarisation vectors. We will discuss these observations later in the context of the origin of the filamentary emission (Section 7.2.2).

We note that in each case when there is a change in the sign of the $\chi - \alpha$, there is an overlapping feature. Examples of this can be seen in Filaments numbers IX, XIV and XIII from Fig. 3, where the first circular aperture closer to the Galactic plane includes emission both from the filament and from the plane, where the field is parallel to the plane. A similar effect can be seen where a filament comes close to another polarised feature away from the plane. See for example the borders of Filament IIIs.

4 POLARISED SPECTRAL INDICES

Temperature spectral indices are useful in identifying the emission mechanism of the measured radiation, thereby, obtain physical properties of the emitting region. Because of the combination of different emitting sources along an arbitrary line-of-sight, it is difficult to measure the spectral index of an individual physical emission mechanism. Davies et al. (2006) selected small regions of the sky that were expected to be dominated by a single emission mechanism, which allowed them to measure the spectral indices of free-free, synchrotron and thermal dust radiation.

Where polarisation data are available, the synchrotron spectral index can be measured unambiguously without the use of component separation techniques in the frequency range below ~ 50 GHz, because the polarisation of the other mechanisms is much smaller. The polarisation of the CMB varies between 1-10%, showing the larger values at small angular scales ($\ell \sim 1000$). Free-free emission

is intrinsically unpolarised (although Thompson scattering could yield a polarisation signal at the edges of HII regions but its contribution to the full sky is less than 1%; [Macellari et al. 2011](#)). Anomalous microwave emission (AME), which is observed at *WMAP* frequencies shows little polarisation. [Dickinson, Peel & Vidal \(2011\)](#) set upper limits of less than 2.6% on the polarisation of two AME regions (see [Rubiño-Martín et al. \(2012\)](#) for a recent review of AME polarisation measurements).

The measurement of precise synchrotron spectral indices has become even more necessary after the discovery of the “haze” by [Finkbeiner \(2004\)](#), a diffuse emission of unknown origin centred at the Galactic centre. [Planck Collaboration et al. \(2013\)](#) indicates the existence of the haze with a spectral index of -2.55 ± 0.05 , favouring a hard-spectrum synchrotron origin for this diffuse emission. This shows that significant synchrotron spectral index variations can occur and they should therefore be measured with care. We note that the foreground-cleaned CMB maps which the *WMAP* team provide are produced on the basis of a fixed spectral index for synchrotron emission. [Fuskeland et al. \(2014\)](#) found variations in the polarisation spectral index between 23 GHz and 33 GHz using *WMAP* data in large regions on the sky.

In this section we measure the spectral index of the bias-corrected polarised intensity between *WMAP* K, Ka and Q bands in a number of regions across the sky using maps smoothed to 3° . We use the T-T plot approach, in which we assume a power-law relationship between the polarised intensities at different frequencies:

$$\frac{T_{v_1}}{T_{v_2}} = \left(\frac{v_1}{v_2} \right)^\beta. \quad (6)$$

This method has the advantage of being independent of any zero level offset or large scale artefacts present in the maps.³ Here, the spectral index β is calculated by fitting a straight line $y = mx + c$ to the measured brightness temperatures T_{v_1} , T_{v_2} :

$$\beta = \frac{\log m}{\log(v_1/v_2)}, \quad (7)$$

where m is the slope of the fit. We took into account the error in both coordinates for the linear fit. Also, an absolute calibration error of 0.2% ([Bennett et al. 2013](#)) has been added in quadrature to the random uncertainty (this corresponds to an uncertainty in β of 0.0076).

In Fig. 7 we show the T-T plots between 23 and 33 GHz for each region. Table 2 lists the location and size of each region, the measured spectral indices, the reduced χ^2 value and the χ^2 probability, q . The T-T plots between K and Ka bands, where the SNR is larger, allow us to measure β with small uncertainties. This occurs mainly on the Galactic plane, where the signal is stronger. At higher latitudes, the fractional uncertainties on the data are larger so the constraints on β are less tight.

We selected the brightest regions from the filaments and also some areas of interest that do not necessarily belong to a filament, including regions on the Galactic plane. Fig. 6 shows the regions that were chosen. Most of them lie in the inner Galaxy and three are in the Fan region, around $l = 140^\circ$, $b = 0^\circ$.

There are a few regions that show a flatter spectral index than the commonly accepted -3.0 value. Regions 1 and 2, at the top of the NPS have $\beta_{K-Ka} > -3.0$ at a $\sim 2\text{-}\sigma$ significance level. Also,

in the Fan region, regions No. 16, No. 17 and No. 18 show a flatter spectral index in at least two pairs of the frequencies used. No polarised sources in these regions are listed in the [López-Cañiego et al. \(2009\)](#) *WMAP* catalogue. On the plane, in the inner Galaxy (regions 11, 12 and 13), the averaged spectral indices are $\beta_{K-Ka} = 3.04 \pm 0.02$, $\beta_{K-Q} = 3.08 \pm 0.02$ and $\beta_{Ka-Q} = 3.15 \pm 0.07$. These values are consistent with the ones measured by [Fuskeland et al. \(2014\)](#) in a larger area on the Galactic plane.

The flatter spectral index in regions No. 1 and 2 between K and Ka bands is interesting as these regions belong to the upper end of the NPS. The flat spectra however, are not observed in β_{K-Q} , which is consistent with -3.0 . These two regions may be interpreted as either an excess of emission in the Ka-band (e.g. from a peaked spinning dust contribution) or as a change in the underlying synchrotron spectral shape, as we can see by the steep values of β_{Ka-Q} . The low significance of the spectral indices measured with the noisier Ka and Q bands do not allow us to draw strong conclusions about these regions at these frequencies. Region number 3, which includes the brighter emission from the NPS has a marginally steeper spectral index $\beta_{K-Ka} = -3.30 \pm 0.15$ than the one measured in total intensity by [Davies et al. \(2006\)](#) of $-3.07^{+0.09}_{-0.13}$ with an angular resolution of 1° . This might indicate the presence of some AME not traced by the templates in the area used in the total intensity analysis.

Regions 4 and 5, which represent the middle and lower region of Filament IX show different spectral indices, with region 5 steeper than region 4 in both β_{K-Ka} and β_{K-Q} . Regions 6 and 7, which represent the middle and lower sections of the GCS also show a similar behaviour, the lower part of the spur has a β_{K-Ka} steeper than the upper section.

The regions closer to the Galactic plane in the inner Galaxy (regions 8, 9, 10, 11, 12, 13 and 14) have values of β_{K-Ka} consistent with -3.0 . These regions represent the area of the sky with the largest amount of polarised emission. A box of 90° degrees in longitude by 20° in latitude centred at $(l, b) = 0^\circ, 0^\circ$, which represents only 4.4% of the total area of the sky encompasses more than 20% of the polarised emission at K band. Hence, this region is particularly significant for the estimation of a full-sky average value of the synchrotron spectral index.

Table 3 lists the weighted mean of the spectral indices from all the regions. There is a hint (close to $2\text{-}\sigma$) of steepening of the spectral index with higher frequencies. The dispersion quoted in Table 3 is large.

5 POLARISATION FRACTION

Calculating the polarisation fraction, Π , of synchrotron emission is a good way to measure the degree of order of the magnetic field perpendicular to the line-of-sight. This calculation is not trivial because of the difficulty in obtaining the synchrotron total intensity at GHz frequencies. Free-free and AME contribute to the total emission so component separation methods are necessary. Here we compare the polarisation fraction at K-band using different templates for the synchrotron intensity over the full sky.

To obtain the polarisation fraction, we measured the ratio, Π , between our debiased polarisation map at K-band (produced using the Wardle & Kronberg estimator from Eq. 2) and a template for the synchrotron intensity at this frequency,

$$\Pi = \frac{P_K}{I_K}. \quad (8)$$

As a first step, we used the total intensity map at K-band only,

³ *WMAP* polarisation maps are affected by poorly constrained modes on very large angular scales ([Jarosik et al. 2011](#)).

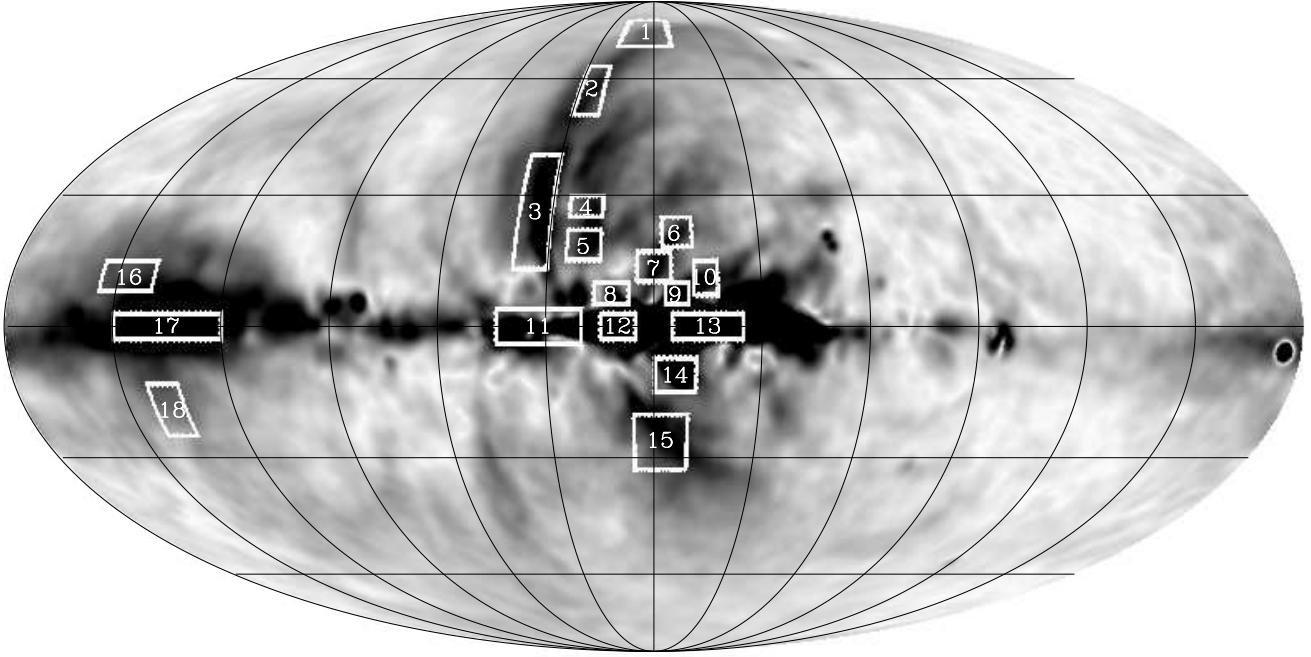


Figure 6. WMAP K-band polarisation intensity map showing the 18 regions chosen to measure spectral indices.

Table 2. Spectral indices in different regions between WMAP K–Ka, K–Q and Ka–Q bands. Also listed are the reduced χ^2 of the fit and the χ^2 probability or q -value, for each T-T plot.

Region	l_0	b_0	l_{size}	b_{size}	β_{K-Ka}	χ^2_{red}	q	β_{K-Q}	χ^2_{red}	q	β_{Ka-Q}	χ^2_{red}	q
1	5.0	75.0	30.0	10.0	-2.29 ± 0.33	0.66	0.90	-3.13 ± 0.47	0.68	0.88	-4.74 ± 1.44	0.80	0.74
2	25.0	57.0	10.0	14.0	-2.12 ± 0.48	1.24	0.20	-3.49 ± 0.92	0.41	0.99	-7.43 ± 3.34	0.61	0.92
3	35.0	26.5	10.0	27.0	-3.30 ± 0.15	0.59	1.00	-3.15 ± 0.16	0.91	0.69	-2.80 ± 0.50	0.80	0.88
4	20.0	27.5	10.0	5.0	-2.70 ± 0.52	0.87	0.60	-2.26 ± 0.45	1.31	0.19	-1.10 ± 1.40	0.66	0.82
5	20.0	18.5	10.0	7.0	-3.61 ± 0.39	0.75	0.79	-2.61 ± 0.30	0.94	0.54	-0.75 ± 1.06	0.87	0.64
6	-6.5	21.5	9.0	7.0	-2.62 ± 0.44	0.43	0.97	-3.04 ± 0.55	1.89	0.02	-3.03 ± 1.52	1.31	0.19
7	0.0	13.5	10.0	7.0	-3.52 ± 0.51	0.88	0.62	-2.34 ± 0.32	1.86	0.01	0.34 ± 1.27	1.55	0.05
8	12.0	7.5	10.0	5.0	-2.89 ± 0.20	0.41	0.98	-3.05 ± 0.24	0.45	0.97	-3.38 ± 0.73	0.60	0.90
9	-6.5	7.5	7.0	5.0	-3.07 ± 0.20	0.69	0.73	-3.13 ± 0.23	2.40	0.01	-3.10 ± 0.68	1.33	0.21
10	-14.5	11.0	7.0	8.0	-3.22 ± 0.36	0.29	0.99	-3.03 ± 0.36	0.18	1.00	-2.75 ± 1.16	0.28	1.00
11*	32.0	0.0	24.0	8.0	-3.08 ± 0.07	1.90	0.00	-3.06 ± 0.07	1.08	0.32	-3.06 ± 0.24	1.16	0.19
12*	10.0	0.0	10.0	6.0	-3.07 ± 0.04	2.10	0.00	-3.06 ± 0.04	1.08	0.36	-3.07 ± 0.12	1.05	0.40
13*	345.0	0.0	20.0	6.0	-3.03 ± 0.02	2.00	0.00	-3.09 ± 0.03	1.12	0.27	-3.20 ± 0.09	0.80	0.83
14	354.0	-11.0	12.0	8.0	-2.84 ± 0.20	0.58	0.95	-3.03 ± 0.25	1.49	0.06	-3.17 ± 0.76	1.11	0.32
15	-2.0	-26.5	16.0	13.0	-3.05 ± 0.28	0.69	0.97	-4.00 ± 0.52	0.83	0.82	-5.89 ± 1.63	0.90	0.71
16	147.5	11.5	15.0	7.0	-2.63 ± 0.38	0.44	1.00	-2.66 ± 0.41	0.69	0.90	-2.43 ± 1.22	0.41	1.00
17*	135.0	0.0	30.0	6.0	-2.64 ± 0.16	1.10	0.26	-2.67 ± 0.16	0.99	0.50	-2.79 ± 0.49	0.93	0.65
18	138.5	-19.0	9.0	12.0	-2.10 ± 0.39	1.15	0.26	-2.37 ± 0.41	1.23	0.19	-3.00 ± 1.29	1.40	0.08

*: These regions are on the Galactic plane.

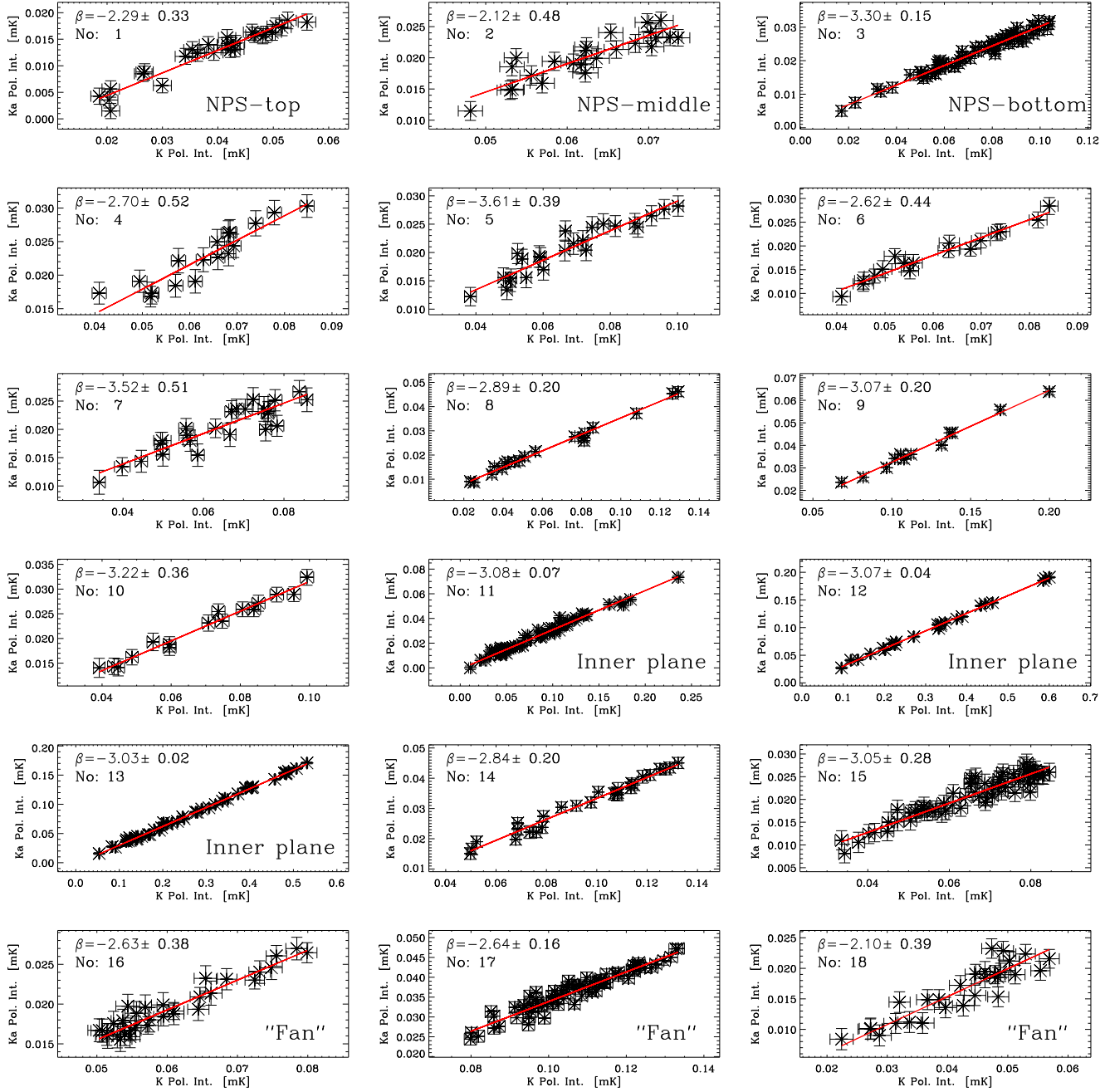


Figure 7. T-T plots of polarisation intensity between 23 and 33 GHz of the eighteen regions defined in Fig. 6. The straight line represents the best linear fit. The error bars show the statistical fluctuations of each point.

which gives a lower limit in Π . We subtracted the contribution from the CMB using the internal linear combination (ILC) map provided by the *WMAP* team (Bennett et al. 2013). The median value over the sky is 9.5% with some regions along the NPS and other filaments showing a value $\Pi \sim 40\%$. This is consistent with a substantial amount of emission from other components beside synchrotron present in the K-band total intensity map.

A way of estimating the synchrotron intensity is by extrapolating the 408 MHz map up to 23 GHz. At 408 MHz there is some free-free coming mainly from star forming regions on the Galactic plane. We subtracted this component by scaling the *WMAP* MEM

Table 3. Weighted average spectral indices and the standard deviation of β for the 18 regions.

	$\bar{\beta}$	σ_{β}
$K - Ka$	-3.03 ± 0.02	0.43
$K - Q$	-3.07 ± 0.02	0.40
$Ka - Q$	-3.17 ± 0.06	1.66

map free-free template to 408 MHz using a free-free spectral index $\beta_{\text{ff}} = -2.13$, valid for the diffuse gas (Davies et al. 2006). Then, we scaled the resulting pure synchrotron map from 408 MHz

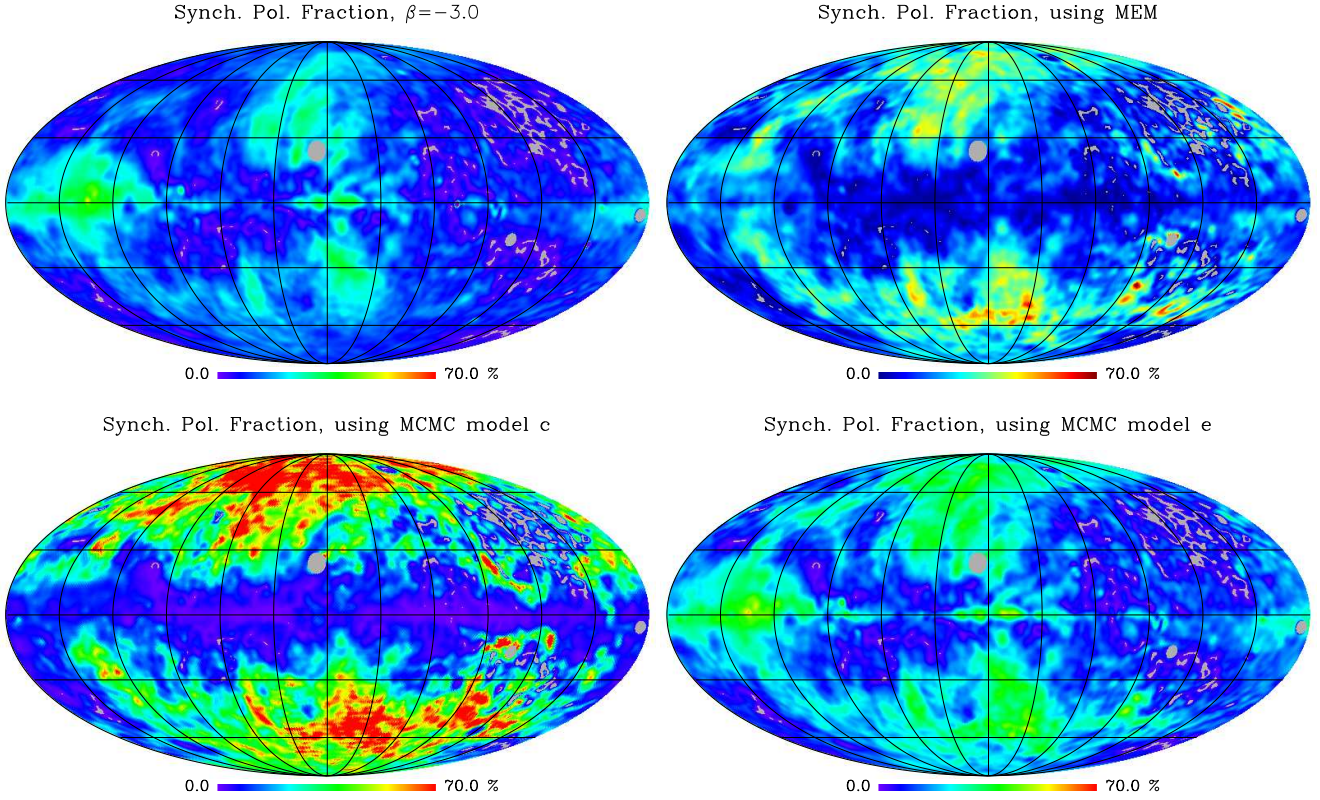


Figure 8. Synchrotron polarisation fraction maps at 23 GHz using different templates for the synchrotron intensity (see text). The colour scale is linear, and it ranges from 0–75%. Our preferred Π map is derived from the *WMAP* MCMC model-e (Gold et al. 2011).

to 23 GHz, using a fixed synchrotron spectral index of $\beta_s = -3.0$. The largest source of uncertainty comes from the fixed synchrotron spectral index between 0.408 GHz to 23 GHz. A variation in the synchrotron spectral from $\beta_s = -3.1$ to $\beta_s = -2.9$ decreases the measured polarisation fraction by a factor ~ 2 . Therefore, accurate measurements of the total intensity spectral index are critical in order to find accurate polarisation fractions using this method.

A second approach to obtain the synchrotron polarisation fraction is based on the modelling of the different emission mechanisms in total intensity. Closer to the plane, there is a large free-free contribution from HII regions so it is necessary to subtract it in order to obtain the synchrotron emission. The *WMAP* team provides all-sky foreground templates at each of the five *WMAP* frequencies, generated using two procedures: Maximum Entropy Method (MEM) and Monte Carlo Markov Chains (MCMC) fits (for a detailed description of the methods, see Gold et al. 2011). The MEM technique generates synchrotron, free-free, spinning dust, and thermal dust templates and assumes that the spectral indices of these foregrounds are constant over the sky. The MCMC method produces four different synchrotron templates, one for each sets of parameters of the prior model. (see Bennett et al. 2013, for a description of the models investigated.) All the methods used to calculate the synchrotron total intensity are listed in Table 4.

We masked three regions on the synchrotron templates that are problematic for calculating the polarisation fraction. First, Tau A ($l = 184^\circ.3$, $b = -5^\circ.8$), where the synchrotron spectral index is flatter ($\beta_s \approx -2.3$) than that observed in the diffuse gas; the ζ Oph HII region ($l = 6^\circ.3$, $b = -23^\circ.6$), where the synchrotron contribution is clearly underestimated in some MCMC models; and an area

from the Gum nebula ($l = 254^\circ.5$, $b = -17^\circ.0$), where the same underestimation of synchrotron occurs. See Figure 8

Fig. 8 shows four out of the six different polarisation fraction maps produced. The differences in these maps are due only to the different synchrotron intensity template used. The extrapolation of the free-free corrected Haslam et al. map (Fig. 8, top-left) produces a Π map which is morphologically very similar to the polarisation intensity map (Fig. 1, top-left), where the structures are filamentary. Regions with high polarisation fraction are individual filaments or specific areas on the plane (e.g. the fan region at $l \sim 140^\circ$). The Π map created using the free-free MEM model (Fig. 8, top-right) has a higher polarisation fraction and also shows a bigger difference between mid and low Galactic latitudes, where the polarisation fraction is near to zero on the plane. The output with the MCMC model e is very similar to the one using the MEM model at high latitudes and to the Haslam map extrapolated close to the plane. It was created with a fixed synchrotron spectral index of -3.0 . MCMC models *c*, *f* and *g* produce very similar and incorrect values for Π , as they result in polarisation fractions $\sim 100\%$ over large areas of the sky at high Galactic latitudes. We therefore believe that these maps are biased over large areas of the sky and we will not discuss further.

Qualitatively, we believe that the best model for the synchrotron total intensity is the MCMC-e model of Gold et al. (2011). This model predicts similar values on the inner Galactic plane and at intermediate latitudes than those calculated extrapolating the Haslam et al. map using $\beta = -3.0$, value similar to the one that we have measured in the same region in Sec. 4. Some regions are highly polarised ($\Pi \approx 30\%$) regardless of the synchrotron model

Table 4. Methods used to estimate the synchrotron total intensity at 23 GHz. Also listed are the median uncertainty over the sky of the polarisation fraction derived from each method, Π_{median} ; the standard deviation along the polarisation fraction maps, Π_{stdev} ; the median of the polarisation fraction at high latitudes ($b > |30^\circ|$), $\Pi_{\text{med}}^{b>|30^\circ|}$ and the median of the polarisation fraction at low latitudes ($b < |30^\circ|$), $\Pi_{\text{med}}^{b<|30^\circ|}$.

Method	Note	Π_{median} [%]	Π_{stdev} [%]	$\Pi_{\text{med}}^{b> 30^\circ }$ [%]	$\Pi_{\text{med}}^{b< 30^\circ }$ [%]
(408 MHz – ff) → 23 GHz	Assumes fixed $\beta_{\text{syn}} = 3.0$.	16.9	10.1	22.0	12.9
WMAP MEM	Includes AME. Fixed $\beta_{\text{syn}} = -3.0$.	11.6	7.6	11.5	11.8
WMAP MCMC model c	No AME component. β_{syn} can vary.	20.5	20.6	36.7	9.9
WMAP MCMC model e	Includes AME. Fixed $\beta_{\text{syn}} = -3.0$	16.2	9.2	18.6	14.0
WMAP MCMC model f	Includes AME. β_{syn} can vary.	21.0	21.6	38.9	9.6
WMAP MCMC model g	Includes AME. β_{syn} varies as described in Strong, Orlando & Jaffe (2011)	22.5	22.6	41.1	10.8

used. Examples are the brighter region of the NPS, the peak of Filament VIIb, the diffuse region in the southern part of Filament Is and Filament IIIs.

6 FARADAY ROTATION

A magnetic field with a component parallel to the line-of-sight will induce the effect of Faraday rotation, in which the plane of polarisation of a travelling photon rotates as it travels through the ISM. The amplitude of the effect depends on the strength of the magnetic field along the line of sight and on the electron density. The observable, the rotation measure RM, is a change in the polarisation angle, χ which scales with the square of the wavelength λ . It is defined as follows,

$$\text{RM} = \frac{d\chi}{d\lambda^2}. \quad (9)$$

If there is a polarised source in the line-of-sight with no intrinsic Faraday rotation, then RM is equal to the Faraday depth, which is defined as (Burn 1966)

$$\phi = \frac{e^3}{2\pi m_e^2 c^4} \int_0^d n_e(s) B_{\parallel}(s) ds, \quad (10)$$

where e and m_e are the electron charge and mass, c the speed of light and the integral is performed over the electron density n_e and the line-of-sight component of the magnetic field B_{\parallel} .

The Faraday rotation at WMAP frequencies is expected to be very small on average. A 1° difference in polarisation angle between K and Ka bands correspond to a rotation measurement of 190 rad m^{-2} . We measured $\Delta\chi$ between K and Ka over most of the sky using the 1° smoothed polarisation maps.

We calculated the polarisation angle rotation for three different signal-to-noise cutoffs (SNR_{cut}). Figure 9 shows the three histograms of the difference between the polarisation angle measured in WMAP –K and Ka bands for three different SNR_{cut} of 3, 5 and 10. The three distributions are centred at zero within the uncertainties. The mean Faraday rotation over the region studied is less than 1° . This value is consistent with the prediction using the Faraday depth map from Oppermann et al. (2012). In the high SNR selection ($\text{SNR} > 10$, blue histogram in Fig. 9), most of the pixels come from the inner Galactic plane. It is here where the Faraday rotation should have its larger effect as the column density is the largest. Nevertheless, on average, the difference in angle measured is consistent with zero. This shows consistency also in the WMAP polarisation angle calibration between K and Ka bands.

The spread in the histograms of Figure 9 is consistent with

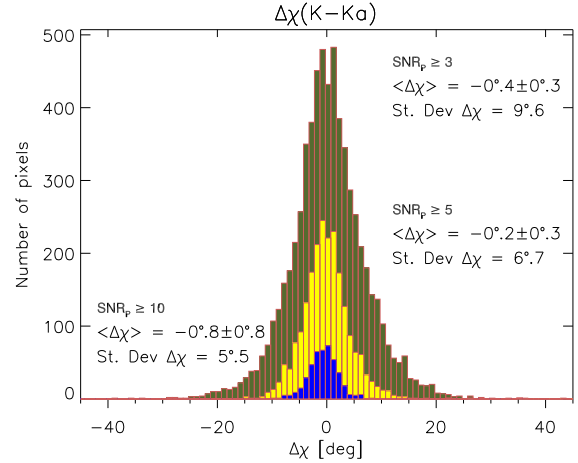


Figure 9. Histograms of the variation in the χ between K-Ka bands using three SNR cuts. The olive histogram is made with the pixels that have $\text{SNR}_p \geq 3$, the yellow histogram with the pixels in which $\text{SNR}_p \geq 5$ and the blue histogram includes pixels that have $\text{SNR}_p \geq 10$. The mean values, uncertainties, and the standard deviations are quoted in the figure for each distribution.

what is expected for a random noise component plus a significant residual. A $\text{SNR}_{\text{cut}} = 3$ is equivalent to an uncertainty in the polarisation angle⁴ of 9.5° , while the measured value using this SNR_{cut} is 9.6° . Table 5 lists the expected width of the histograms for each SNR cut for a noise only component. It also shows the observed width of the histograms and the difference between these two values, which can be attributed to Faraday rotation. We note that this difference is actually a slight underestimate of the true dispersion because some pixels will have SNR larger than the cutoff. The region with the higher SNR cut (pixels in the blue histogram of Fig. 9) has the widest residual distribution of 4.7° , which corresponds to a rotation measures of $\pm 893 \text{ rad m}^{-2}$. However, this region represents only 0.9% of the area of the sky. Figure 10 shows the difference in polarisation angle between K and Ka bands in the inner Galaxy. Here, the Galactic centre shows significant amount of Faraday rotation with a peak value of $\Delta\chi_{\text{K-Ka}} = 34^\circ$ at the central pixel.

⁴ Ignoring QU correlations, $\sigma_\chi = \sqrt{Q^2\sigma_Q^2 + U^2\sigma_U^2}/P = (2\text{SNR}_p)^{-1}$.

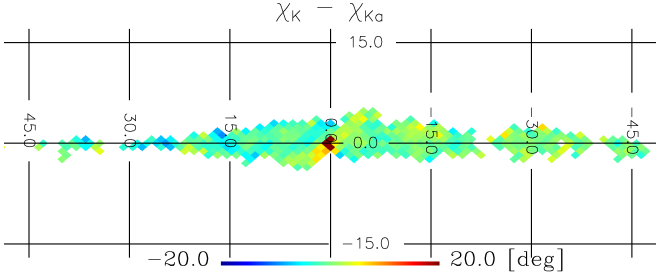


Figure 10. Difference in polarisation angle between *WMAP* K and Ka bands in the inner Galaxy. Only the pixels where the SNR in the polarisation angle is greater than 10 are shown. The central pixels shows a peak value of $\Delta\chi_{K-Ka} = 34^\circ$.

Table 5. For three different SNR cut values, we list the fraction of the sky which is used, the width of the distribution expected for a noise only contribution $\sigma_{\chi-\text{noise}}$, the observed width of each distribution, shown in Figure 9 and the difference between these two widths, $\sigma_{\text{Faraday}}^2 = \sigma_{\Delta\chi}^2 - \sigma_{\chi-\text{noise}}^2$, which can be attributed to Faraday rotation.

SNR _p	Sky fraction [%]	$\sigma_{\chi-\text{noise}}$	$\sigma_{\Delta\chi}$	σ_{Faraday}
3	13.1	9°5	9°6	1°4
5	4.3	5°7	6°7	3°5
10	0.9	2°8	5°5	4°7

7 DISCUSSION

We have presented a range of observational parameters that can be drawn from the *WMAP* polarisation data. We have seen that an important part of the polarised emission at microwaves comes from filamentary structures at high Galactic latitudes. What is the origin of these filaments? How do they relate with the rest of the ISM, the neutral gas for example? We start this discussion by looking at HI data, which traces the neutral gas of the Galaxy. We then go through the hypothesis for the origin of these filaments and use *WMAP* data to test the predictions of one model.

7.1 HI morphology

Most of the filamentary features that extend roughly perpendicular to the Galactic plane lie in the inner Galaxy, with $|l| \lesssim 60^\circ$. In these structures, the polarisation angle is roughly aligned along the extension of the filaments. The top panel of Fig. 11 shows the inner region of the Galaxy between $|b| < 30^\circ$ visible in K-band polarisation.

These structures appear similar to the HI “worms” described by Heiles (1984); Koo, Heiles & Reach (1992). Heiles proposed that these worms observed in the inner Galaxy are shells with open tops. Stellar winds and supernova explosions create shells in the ISM and if the expansion energy is large enough, hot gas will flow out through chimneys to the Galactic halo. Chimney walls are vertically supported by magnetic fields (Breitschwerdt, McKenzie & Voelk 1991), which can glow in radio continuum if cosmic rays diffuse through them.

Sofue (1988) describes a number of radio spurs present in the 408 MHz map of Haslam et al., and most of these spurs lie in the inner Galaxy. He did not find definitive correlations between HI and the radio continuum structures in this region. Here, we examine the more sensitive HI 21 cm maps from the Leiden/Argentine/Bonn (LAB) survey Kalberla et al. (2005), which maps the full sky with

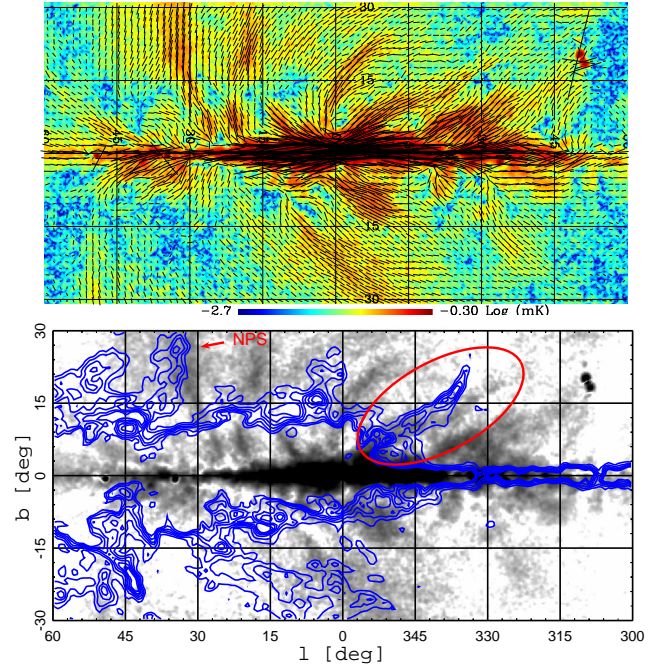


Figure 11. *Top:* *WMAP* K-band polarisation intensity map showing the inner Galaxy between $l = \pm 60^\circ$. The polarisation vectors are rotated by 90° to indicate the direction of the magnetic field. *Bottom:* Same as the map on *Top*: but using a linear colour scale. The contours of HI 21 cm emission at $v = +10 \text{ km s}^{-1}$ are shown in blue. There is a possible association between the HI and the polarised intensity on filament XIV. The angular resolution is 1° and the graticule has 15° spacing in both Galactic coordinates. Both maps are centred at $(l, b) = (0^\circ, 0^\circ)$.

an angular resolution of 36 arc min FWHM in the velocity range from -450 km s^{-1} to $+400 \text{ km s}^{-1}$, at a resolution of 1.3 km s^{-1} . We searched for morphological correlations between the polarisation spurs and the HI velocity maps. We did not find obvious correlations either. The only features that have HI counterpart are the NPS and the polarised filament No. XIV in our nomenclature. Fig. 11 (*bottom*) shows the polarisation map with the HI contours of the velocity range that shows the correlation. From the figure, we can see that the correlation is better near the base of the filament and with increasing latitude, there is a spatial separation in the HI emission from the polarised synchrotron. This HI filament in particular is part of a larger shell, probably the limb-brightened periphery of a HI bubble. This is visible in the *top* panel of Fig. 12 where we show the full sky HI map with a velocity of $+10 \text{ km s}^{-1}$, where there is a shell-like structure of $\sim 30^\circ$ in diameter centred around $(l, b) = (350^\circ, 20^\circ)$.

If the polarised emission that comes from filament No. XIV is indeed physically correlated with the HI emission from this bubble, this would resemble the Heiles (1984) picture previously described. Here, an enhancement in the magnetic field, produced by the compression of the ambient field by an expanding shock, can induce the emission of polarised synchrotron radiation along the field lines.

We now draw attention to the structure centred at $l \sim 320^\circ$ on the plane, the large shell that is most visible at -10 km s^{-1} (*bottom* panel of Fig. 12). This shell is known as the Scorpius-Centaurus super-shell, a cavity in the local ISM which is thought to be the expanding remnants of a number of SNe explosions (e.g. Weaver 1979). Inside this cavity lies the Sco-Cen OB association, the nearest group to the Sun containing massive stars, where the distances

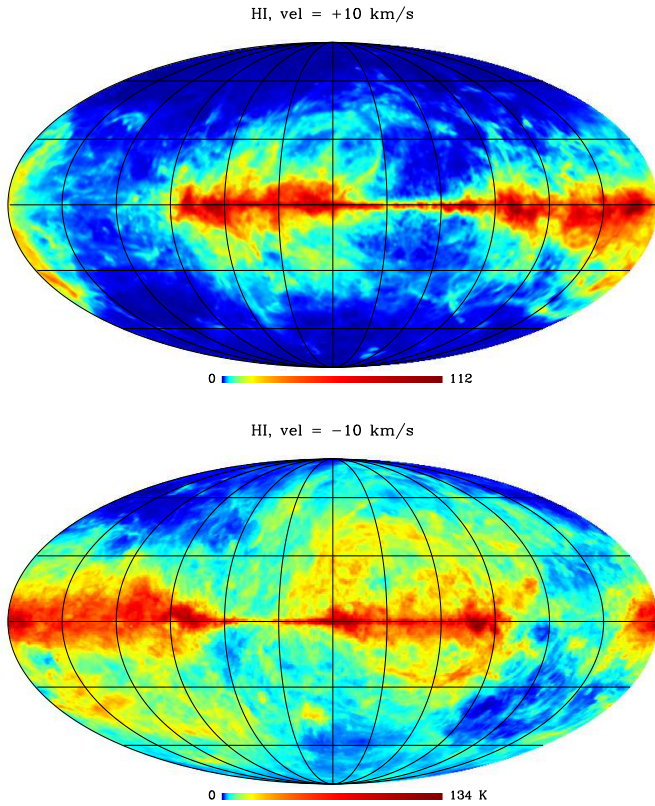


Figure 12. HI maps of the full sky at two line-of-sight velocities from the LAB survey (Kalberla et al. 2005): $+10 \text{ km s}^{-1}$ (top) and -10 km s^{-1} (bottom). The graticule has 30° spacing in both Galactic coordinates and the maps are plotted using a histogram-equalised scale.

of its members lie between 118 and 145 pc and the oldest groups of stars are $\sim 15 \text{ Myr}$ old (Preibisch & Mamajek 2008). We note that the HI counterpart of the NPS lies on the periphery of the Sco-Cen shell. We will discuss this connection in more detail in the next section.

7.2 Large scale polarised loops origin: towards a possible model

7.2.1 Background

Since the early attempts to explain the origin of the radio continuum loops, SN remnants expanding in the Galactic magnetic field have been a preferred alternative. Spoelstra (1971, 1972, 1973) applies the model of a sphere expanding in the ISM by van der Laan (1962) to Loops I, II, III and IV. In this model, the compression of the magnetic field due to the shock wave from the SN will act as a synchrotron source. The emission will be more easily observable on the periphery of the shell due to limb-brightening, which explains the loop-type shape of the remnants.

Sofue, Hamajima & Fujimoto (1974) discuss a number of difficulties that this SNR hypothesis faces to explain diverse observational data. They present a new model in which the spurs are the result of the tangential view of a region of shocked gas produced at the spiral arms that extends above and along the arms. This hypothesis explains the origin of Loops II and III and many other spurs according to the authors. The NPS on the other hand, can be explained according to Sofue (1977) in terms of a magnetohy-

drodynamical phenomenon associated with the Galactic centre. A similar scenario connected to the Galactic centre was more recently proposed by Bland-Hawthorn & Cohen (2003), based on diffuse filamentary infra-red emission observed on both sides of the Galactic plane, which is thought to be formed by a central outburst with an energy scale $\sim 10^{55}$ ergs. This interpretation implies that the spur has a kpc scale, in comparison with the hundred-pc scale that is expected from the SNR hypothesis.

It is clear that a distance determination for the spurs was necessary to settle which interpretation was correct. Bingham (1967), using optical polarisation data, which is correlated with the polarised emission from the NPS, determined a distance of $100 \pm 20 \text{ pc}$. The discovery of HI emission from the periphery of the NPS in the maps of Heiles (1974) and Colomb, Poppel & Heiles (1980) has also helped in this matter. Puspitarini & Lallement (2012) have shown that HI gas that belongs to the top region ($b \geq +70^\circ$) of Loop I is located at a distance of $98 \pm 6 \text{ pc}$ and the material at intermediate latitudes ($+55^\circ \leq b \leq +70^\circ$) is around 95–157 pc. This is strong evidence that favours a nearby shell as the origin of Loop I.

In this nearby scenario, a problem with a single SN event as the origin for Loop I is the discrepancy on the expected age for such SN event. The low expanding velocity of the HI gas, $|v| \leq 20 \text{ km s}^{-1}$ (Sofue, Hamajima & Fujimoto 1974; Weaver 1979; Kalberla et al. 2005), implies an SN older than several 10^6 yr . On the other hand, soft X-ray emission detected from the interior of the radio loop by Bunner et al. (1972) suggest an age 10 times younger. Moreover, the initial SN energy in either case is $\sim 10^{52}$ ergs, an order of magnitude larger than the standard 10^{51} ergs (Egger & Aschenbach 1995).

A related scenario in which instead of a single SN event, the Loop I cavity is a super-bubble, the result of stellar winds and consecutive supernovae in the Sco-Cen OB association is more attractive. This idea has been suggested by a number of authors, (see e.g. Weaver et al. 1977; Heiles et al. 1980). Egger (1995) present a model in which a recent SN inside the Sco-Cen super-shell shocks the inner walls of the bubble, giving rise to the NPS emission.

An expanding super-shell in a magnetised medium has been modelled by Tomisaka (1992). In their model, during the early stages of the shell (a few Myr), the expansion is spherically symmetric. In a later phase ($\sim 50 \text{ Myr}$), the magnetic field stops the expansion perpendicular to the field lines producing a highly elongated bubble. Cosmic rays accelerated by the shock will emit polarised synchrotron travelling through the distorted field lines produced by the shell.

7.2.2 A proposed model

Assuming that the unperturbed magnetic field lines in the vicinity of the Sun are parallel to the Galactic plane, an expanding super-shell will bend the lines in a simple manner. The originally parallel field lines will follow lines of constant longitude on the surface of the expanding sphere. The observed pattern from Earth however is not trivial and it will depend on the viewing angle of the shell. Following what Heiles (1998) showed using starlight polarisation, we can compare the direction of the field lines in this scenario, produced by a shell centred at the location of the Loop I bubble, with the polarisation angle of the emission seen by WMAP. This type of modelling was also used by Wolleben (2007), who placed two overlapping shells that deforms the magnetic field medium to reproduce the polarisation directions observed at 1.4 GHz. These data show a depolarisation band confined at $|b| \approx 30^\circ$, so their fit is based only on the high latitude data. The low Faraday rotation

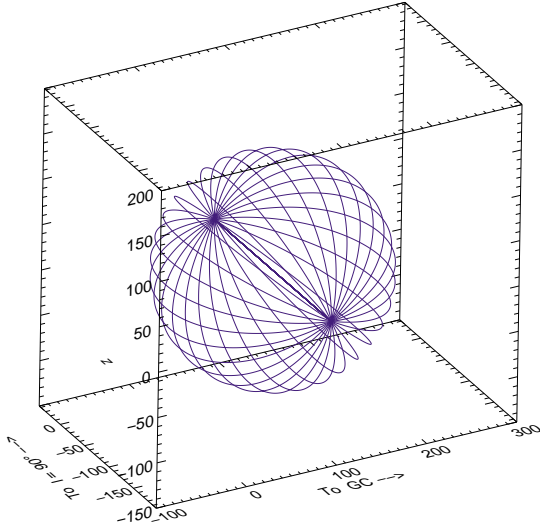


Figure 13. Direction of the magnetic field lines on the surface of a spherical shell expanding in a magnetised medium with an initial uniform field parallel to the Galactic plane. The field lines will follow “meridian” lines on the surface of the shell as it is shown in the figure. The Sun is located at the origin of the three axes and the units of are parsecs. The radius of the shell is 120 pc and it is located at 120 pc from the Sun in the direction $(l, b) = (320^\circ, 5^\circ)$.

of the *WMAP* data allow us to compare directly the angles in the $|b| \leq 30^\circ$ band, where there is strong emission from the spurs.

We locate the centre of the bubble at 120 pc, in the direction of the Sco-Cen supper shell as seen in H I at $(l, b) = (320^\circ, 5^\circ)$ (Heiles 1998). We note that this is not the centre of the Loop I as measured in radio data (table 1) Fig. 13 shows a 3D projection of the field lines on the surface of the shell. From the figure, it is clear that the vantage point will define the appearance of the field lines for any observer.

A Mollweide projection of the view of the field lines onto the sky is shown in Fig. 14. The lines closer to the “poles” of the sphere have been masked to avoid crowdedness. In Figure 15 we compare the predicted polarisation angle direction vectors (in red) on top of the *WMAP* K-band polarisation vectors. It is remarkable that this very simple model fits very well the direction of the largest loops, above the Galactic plane. The bottom panel of Fig. 15 shows the pseudovectors from starlight polarisation measurements, taken from the Heiles (2000) compilation. We only selected the stars with distances less than 300 pc. There is also very good agreement between the structures seen in starlight polarisation with the polarisation vectors from *WMAP* and our model (top panel of the Fig. 15), particularly at the Northern Galactic hemisphere, at the interior of Loop I. This is good evidence that the common structures between the two maps are nearby structures, as we only used stars within a 300 pc radius to create the map.

In this scenario, where the emission comes from the compression of the interstellar field lines, one would expect emission coming from most of the surface of the shell. This is clearly not the case. The NPS and the other large loops are the only places where there is a significant amount of synchrotron. The reason for this difference in synchrotron emission on different regions might be connected with the density of the ISM at different sides of the shell. The interaction of the shell with a denser medium might trap cosmic rays more efficiently than in a less dense environment. Lalle-

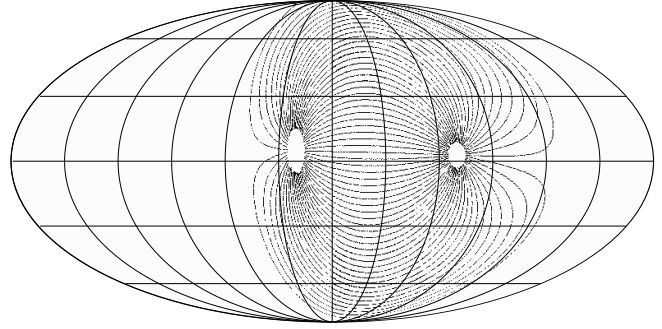


Figure 14. Projection on the sky of the magnetic field lines directions of a spherical shell of 120 pc of radius located at 120 pc in the direction. The grid spacing is 30° in both l and b .

ment et al. (2003) presented a 3D map of the nearby ($d \lesssim 500$ pc) ISM by mapping the absorption of Na lines by neutral interstellar gas using 1000 lines-of-sight. The section of the shell that has higher emission, corresponding to the NPS, is close to the denser Ophiuchi clouds, while the rest of the shell is expanding into a tenuous low density cavity. The difference in local density might be responsible for the different synchrotron emissivity along the shell.

Mertsch & Sarkar (2013) analysed the angular power spectrum of the diffuse synchrotron emission as observed in the Haslam et al. map. They compared the observed power spectrum with a modelled one, which includes $O(1000)$ SN shells distributed in the Galaxy with scales ~ 100 pc. The inclusion of these SN shells greatly improves the fit of the power spectrum. If the results from their modelling are correct, these shell-like structures are quite common in the Galaxy, supporting the idea of an SN remnant origin for the diffuse synchrotron radiation.

We think that the model discussed here, which implies a nearby origin for Loop I and the largest filaments, describes the data better than the models connecting these large filaments with activity from the Galactic centre. One of the arguments that Bland-Hawthorn & Cohen (2003) use to connect the NPS with nuclear activity is that the radio continuum emission from the NPS is thermal, originated by a shock-induced UV field which ionized the gas. The spectral indices measured in this work show the opposite, a steep spectral index consistent with diffuse synchrotron emission. Also, the polarisation observed is the signature of synchrotron and not free-free emission. In another work, Jones et al. (2012) claim that the magnetic field is perpendicular to the extension of the GCS and hence is consistent with a toroidal magnetic field along the spur. This is an error, as we have shown that the field is actually parallel. We have recreated their plot of the *WMAP* data by replacing Q, U by $-Q, -U$; but to show the magnetic field direction $-Q, -U$ must be used.⁵ As the magnetic field lines are parallel to the extension of the filament, a toroidal field along the spur can be ruled out. Carretti et al. (2013), with polarisation data at 2.3 GHz, detected two polarised radio lobes that encompass around 60° in the inner Galaxy. They claim that the origin of these lobes is connected with a large star formation activity in the central 200 pc of the Galaxy that can transport $\sim 10^{55}$ ergs of energy into the Galactic halo. This interpretation includes the emission from the GCS, NPS-S, filaments VIII and IX from our analysis. We remark that this hypothesis is

⁵ The same error would occur if *WMAP* $-Q, -U$ were plotted in a package assuming the normal (IAU) sign convention for Stokes U , since *WMAP* uses the cosmological convention with the opposite sign.

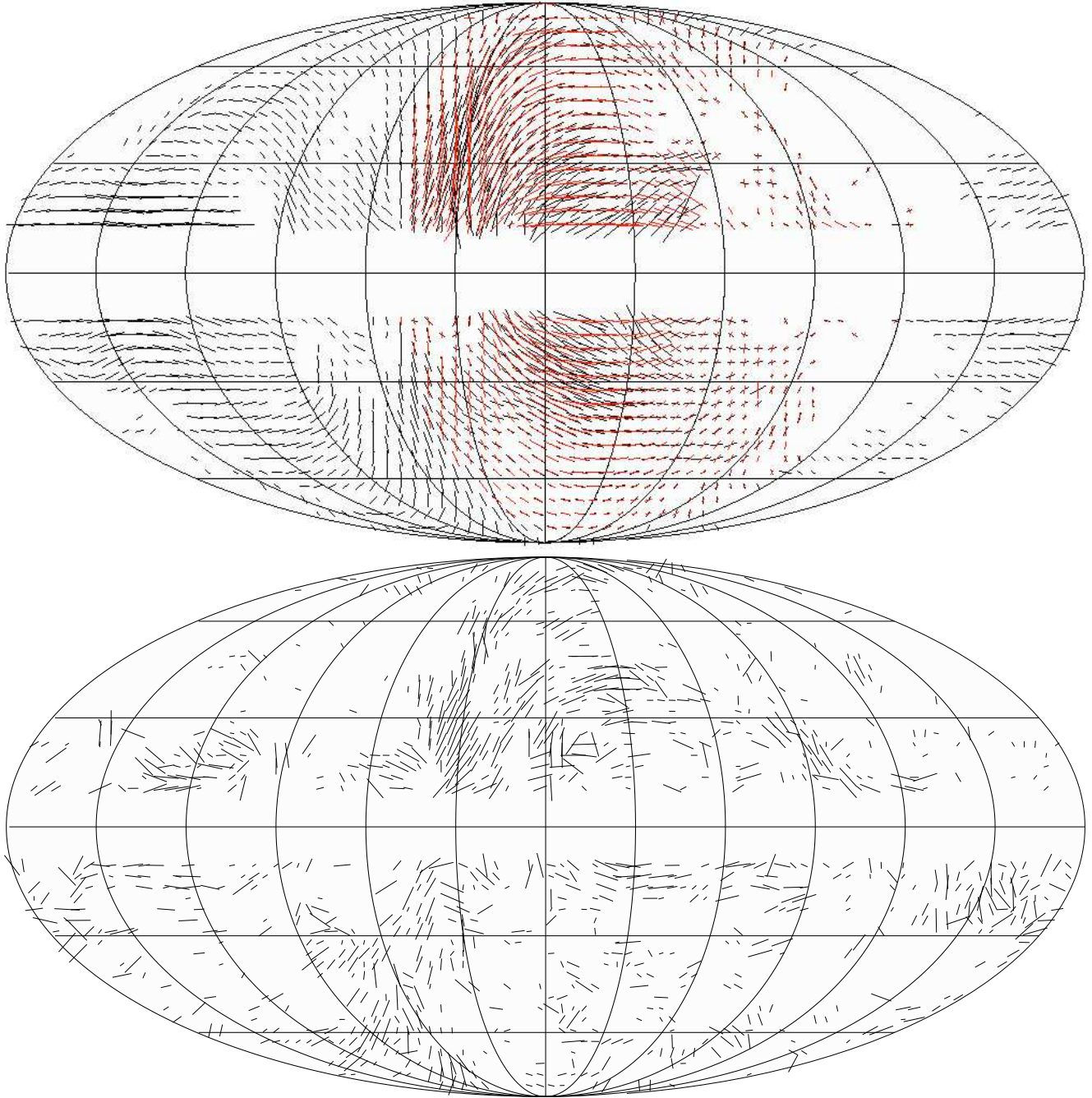


Figure 15. *Top:* Comparison between the predicted polarisation vectors using the field lines shown in Figure 14 in red and the the polarisation vectors observed by WMAP at K-band in black. The red vectors have been scaled to have the same amplitude as the polarisation observed at K-band. *Bottom:* Pseudovectors representing the polarisation angle from starlight polarisation measurements, taken from the Heiles (2000) compilation. The grid spacing is 30° in both l and b .

not incompatible with the existence of the local shell that we have discussed here.

If the large-scale polarisation pattern is due to local features, as it seems to be the case, it cannot be used to test global models of the Galactic magnetic field. Large scale modelling of Faraday rotation and other polarisation data has been attempted in a number of works Page et al. (2007); Han (2009); Taylor, Stil & Sunstrum (2009); Mao et al. (2012). But, as shown here, the locally measured high-latitude polarizations and Faraday rotations result from local structures, not from the large-scale global Galactic magnetic field

structure. This is a very important consideration that has to be taken into account in further modelling of the Galactic field structure of the Galaxy.

We note with interest that Clark, Peek & Putman (2014) have recently found much smaller-scale ($10'$) filaments in the atomic hydrogen distribution, which also align with the local magnetic field. They show that most of their filaments lie outside the local cavity, at distances larger than 100 pc. This is in agreement with the model that we studied here, as the fibres would be aligned by the

same mechanism, where the local magnetic field is distorted by an expanding shell.

In summary, we have used a simple model, based on the idea from Heiles (1998) where an expanding shell is deforming the local magnetic field to explain the large scale polarisation features seen by *WMAP*. There is a very good agreement between the polarisation direction predicted from the model with the *WMAP* data, as can be seen in Fig. 15, and also with the polarisation orientation as measured by starlight observations. We remark that this good correlation with the starlight only occurs when the selected stars are nearby, i.e. $d \lesssim 300$ pc. This is good evidence that the magnetic structures that give rise to the polarisation observed by *WMAP* is of local origin. We also note that a large number of the filaments described in Sec. 3 are represented by this model. This means that some of the filaments, such as I, Is, IX, CGS, CIV, XIII, VIII, XII, XII and XI from Fig. 2 are likely to be part of the same local structure. In order to get a more clear picture, the *Planck* polarisation is very valuable as it provides polarisation data sets both at low frequency, tracing the synchrotron emission and also, more importantly, full sky polarisation maps of the dust emission, which could be related with HI data. This analysis however is outside the scope of this paper.

7.3 CMB foreground contribution

With the aim of quantifying the contribution of the polarised filaments in the context of foreground to the CMB, we have calculated the power spectra of the polarised synchrotron sky. Using masks which include/remove the observed filaments, we calculate the spectra and then compare these with the expected E and B-modes components of the CMB, to assess the level of contamination that the filaments induce at different angular scales. Recently, Liu, Mertsch & Sarkar (2014) suggested that the radio Loops can also be traced at high frequencies by polarised dust emission so there might be significant CMB foreground contamination at their location.

In order to test the contribution of the filaments to the power spectrum of the full sky, we calculated the BB spectrum of the *WMAP* K-band polarisation maps using two different masks: one that suppresses all the pixels on a 10° strip on the Galactic plane and a second mask that masks out the polarised features at high latitudes. These masks can be seen in Fig. 16.

The power spectrum was computed using the publicly available PolSpice package (Chon et al. 2004). This software measures the the angular auto- and cross- power spectra $C(l)$ of Stokes I , Q and U . It is well suited for our applications because it can correct for the effects of the masks, taking into account inhomogeneous weights given to the pixels of the map. The mixing of the E and B modes due to the masked sky and pixel weights is corrected for, so an unbiased estimate of the B-mode spectrum is given.

We also calculated a theoretical CMB power spectrum using the CAMB package (Lewis, Challinor & Lasenby 2000). For this, we used the cosmological parameters from the *WMAP* 9-year release, listed in Hinshaw et al. (2013). We used a tensor-to-scalar ratio $r = 0.2$ for the B-mode spectrum calculation based on the recent measurement by the BICEP2 collaboration⁶ (BICEP2 Collaboration et al. 2014). We calculated the power spectrum for two differ-

⁶ We note that there has been considerable debate about whether this detection is contaminated by foregrounds (Flauger, Hill & Spergel 2014; Mor-tonson & Seljak 2014), which may result in a much lower value for r .

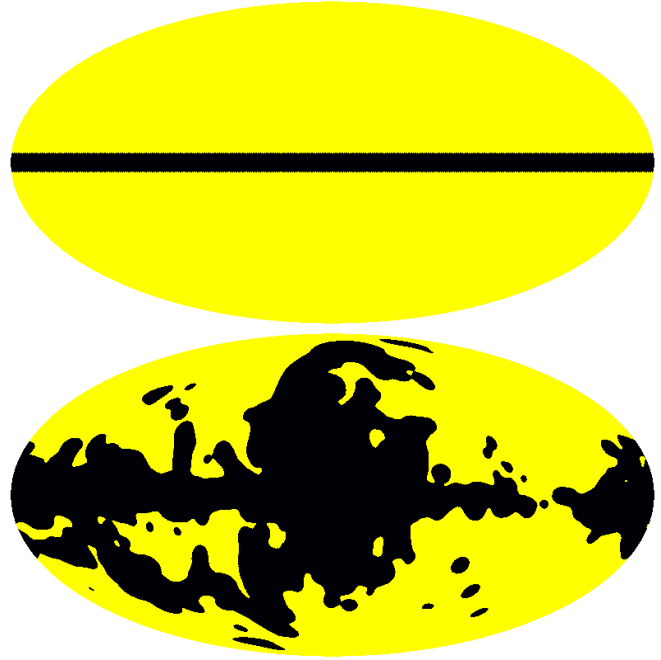


Figure 16. The two mask used in the analysis. On the *top* is the one that masks the Galactic plane, all the pixels where $|b| \lesssim 5^\circ$ and it covers $\approx 7\%$ of the sky. On the *bottom* is the one that we used to mask the emission from the filaments. This masks covers $\approx 27\%$ of the sky.

ent frequencies. First, at 23 GHz, where the polarised synchrotron is expected to dominate and also at 150 GHz, where its contribution is significantly reduced. Because we aim to estimate the contribution of the synchrotron filaments, we do not include any dust contribution at these higher frequencies. We used a polarised spectral index of $\beta = -3.0$ to scale the emission from 23 to 150 GHz. This value is an average for the high latitude filaments as we have derived previously. We note that β_{23-150} might be steeper than the -3.0 value that we used due to a possible frequency steepening of the spectrum. If this occurs, the contribution that we show here at 150 GHz will be an overestimate for the power of the synchrotron filaments at 150 GHz.

In Fig. 17 we show the resulting polarisation power spectrum at 150 GHz. The black lines shows the expected B-mode, including the primordial and a lensing component. The red line show the B-modes spectrum of the polarised synchrotron map computed using only the Galactic plane mask, while the blue lines show the spectrum computed using the filaments mask. The difference between the spectra calculated using these two masks is more pronounced at the large angular scales (low multipole value), as expected given the extension of the filaments. The B-mode power calculated using the filament mask is ~ 10 times smaller for $\ell = 5$ than the power estimated using only the Galactic plane mask. With increasing multipole value, the difference of the spectra calculated with the different masks is smaller. The large difference at low- ℓ on the B-modes spectrum is important because the “low- ℓ bump” of the CMB B-modes spectrum will be a target for the experiments that aim to detect the cosmological B-mode signal (see e.g. Katayama & Komatsu 2011). However, at 150 GHz the synchrotron power is expected to be small compared with the B-modes spectrum if $r = 0.2$. We note that the last bins in the power spectrum are noise dominated.

The poorly-constrained modes in the *WMAP* polarisation data

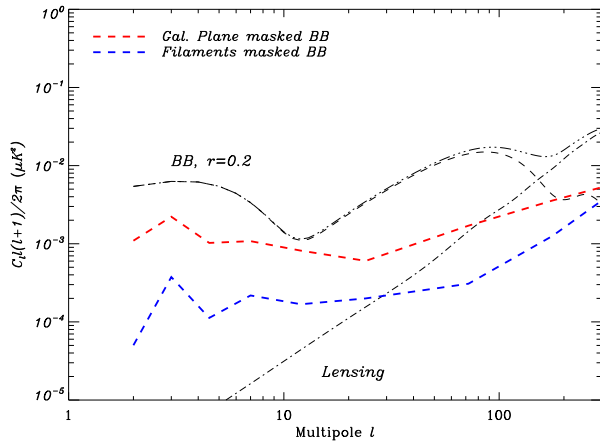


Figure 17. B-modes power spectra for the polarised synchrotron component at 150 GHz compared to the theoretical CMB B-modes spectrum. In black are the CMB spectra where the B-modes were calculated using a tensor-to-scalar ratio value of $r = 0.2$. In colour are the B-mode spectra of the synchrotron polarisation map calculated using the two masks shown in Fig. 16. The dot-dashed line shows the contribution from lensing to the cosmological B-mode spectrum.

will give excess power at $\ell \lesssim 8$ (Jarosik et al. 2011). In the *WMAP* analysis, these were explicitly downweighted in the power spectrum estimation, but we have not done this. This implies that our power spectrum is slightly high in this multipole range.

8 CONCLUSIONS

The polarised sky at 23 GHz is dominated by synchrotron emission and, away from the Galactic plane, it originates mostly from filamentary structures with well-ordered magnetic fields. Some of these structures have been known for decades in radio continuum maps: the “radio loops”, with the North Polar Spur being the most studied. The origin of these filaments is not clear and there are many filaments that are visible for the first time in these polarisation data. We have identified 11 filaments, including three of the well known radio continuum loops. Five of these filaments are only visible in the polarisation data. The geometry of these filaments can be described using circular arcs. We fitted for the centres and radii of these “loops”. We also compared polarisation angles along the filaments with the direction defined by their extension. The polarisation angle is well aligned along the filaments, being typically tangential to their direction. We found however some systematic differences between the polarisation angle χ and the direction defined by the extension of the filament.

We measured the polarisation spectral indices of 18 small regions in the sky and we found significant variations in β over the sky. Some of the regions show a spectral index flatter than the usual $\beta = -3.0$, for example the Fan region, around Galactic longitude $l = 140$, which shows $\beta_{K-Ka} = -2.68 \pm 0.16$. On average, no significant steepening with frequency of the spectral index is observed between β_{K-Ka} and β_{Ka-Q} , although some individual regions do show some steepening, such as some regions on the Galactic plane. The average spectral index in all the 18 regions considered is $\beta_{K-Ka} = -3.04 \pm 0.02$.

We quantified the polarisation fraction of the synchrotron emission over the entire sky, using different templates to estimate

the synchrotron total intensity at 23 GHz. The results depend critically on the model used for the synchrotron total intensity. Nevertheless, some of the polarised filaments show a large polarisation fraction ($\Pi \approx 30\%$) regardless of the synchrotron total intensity template used.

We measured the Faraday rotation between K and Ka bands at an angular resolution of 1° . We only find signs of Faraday rotation on the inner Galactic plane. Here, the change of polarisation angle between K and Ka bands has an rms value of 4.7° , corresponding to a rotation measure of 890 rad m^{-2} . This region however, covers only 0.9% of the total area of the sky. Over most of the sky, the difference in polarisation angle between K and Ka bands is less than 1° ($\text{RM} = 190 \text{ rad m}^{-2}$).

To explain the large-scale observed polarisation pattern, we invoke a model originally proposed by Heiles (1998), in which an expanding shell, located at a distance of 120 pc compresses the magnetic field in the local ISM. Under the assumption that the unperturbed magnetic field lines are parallel to the Galactic plane, an expanding spherical shell will bend the lines in a simple manner. We calculated how these field lines would appear from our vantage point within the Galaxy. The predicted direction of the magnetic field lines is in good agreement with the observed polarisation angles at 23 GHz for most of the relevant area of the sky. We highlight that this model includes emission from many of the observed filaments, therefore connecting them as part of a big local structure. This result suggests that a substantial part of the filamentary and diffuse emission seen by *WMAP* is local. This has to be taken into account when trying to model the global Galactic polarisation emission and magnetic field.

Finally, we estimated the level of contamination that the filaments add to the CMB E- and B-mode power spectra. We compared the B-mode power spectrum of the sky at 23 GHz using two different masks, one that covers only the Galactic plane and a second one that masks-out the diffuse filaments. The power measured at $\ell = 3$ using the Galactic plane masks is ~ 10 times larger than the power measured using the filaments mask. This implies that a careful subtraction is required to precisely measure the CMB B-mode spectrum at the largest angular scales.

ACKNOWLEDGEMENTS

We thank the referee, Carl Heiles, for his comments and suggestions that have greatly improve the quality of the paper. We thank Anthony Banday and Michael Keith for some very useful comments on this work. MV acknowledges the funding from Becas Chile. CD acknowledges an STFC Advanced Fellowship, an EU Marie-Curie IRG grant under the FP7 and ERC Starting Grant (no. 307209). We acknowledge the use of the Legacy Archive for Microwave Background Data Analysis (LAMBDA). Support for LAMBDA is provided by the NASA Office of Space Science. Some of the work of this paper was done using routines from the IDL Astronomy User’s Library⁷. Some of the results in this paper have been derived using the HEALPix (Górski et al. 2005) package.

REFERENCES

- Ackermann M. et al., 2012, *ApJ*, 750, 3
- Adriani O. et al., 2011, *Physical Review Letters*, 106, 201101

⁷ <http://idlastro.gsfc.nasa.gov/>

- Banday A. J., Wolfendale A. W., 1991, *MNRAS*, 248, 705
- Bennett C. L. et al., 2013, *ApJS*, 208, 20
- Berkhuijsen E. M., 1973, *A&A*, 24, 143
- Berkhuijsen E. M., Haslam C. G. T., Salter C. J., 1971, *A&A*, 14, 252
- BICEP2 Collaboration et al., 2014, *ArXiv e-prints*
- Bingham R. G., 1967, *MNRAS*, 137, 157
- Bland-Hawthorn J., Cohen M., 2003, *ApJ*, 582, 246
- Borka V., 2007, *MNRAS*, 376, 634
- Breitschwerdt D., McKenzie J. F., Voelk H. J., 1991, *A&A*, 245, 79
- Brown R., Davies R. D., Hazard C., 1960, *The Observatory*, 80, 191
- Bunner A. N., Coleman P. L., Kraushaar W. L., McCammon D., 1972, *ApJ*, 172, L67
- Burn B. J., 1966, *MNRAS*, 133, 67
- Carretti E. et al., 2013, *Nature*, 493, 66
- Chon G., Challinor A., Prunet S., Hivon E., Szapudi I., 2004, *MNRAS*, 350, 914
- Clark S. E., Peek J. E. G., Putman M. E., 2014, *ApJ*, 789, 82
- Colomb F. R., Poppel W. G. L., Heiles C., 1980, *A&AS*, 40, 47
- Davies R. D., Dickinson C., Banday A. J., Jaffe T. R., Górski K. M., Davis R. J., 2006, *MNRAS*, 370, 1125
- Dickinson C. et al., 2009, *ApJ*, 705, 1607
- Dickinson C., Peel M., Vidal M., 2011, *MNRAS*, 418, L35
- Dunkley J. et al., 2009, *ApJ*, 701, 1804
- Egger R. J., 1995, in *Astronomical Society of the Pacific Conference Series*, Vol. 80, *The Physics of the Interstellar Medium and Intergalactic Medium*, Ferrara A., McKee C. F., Heiles C., Shapiro P. R., eds., p. 45
- Egger R. J., Aschenbach B., 1995, *A&A*, 294, L25
- Finkbeiner D. P., 2004, *ApJ*, 614, 186
- Flauger R., Hill J. C., Spergel D. N., 2014, *Journal of Cosmology and Astroparticle Physics*, 8, 39
- Fuskeland U., Wehus I. K., Eriksen H. K., Næss S. K., 2014, *ApJ*, 790, 104
- Giardino G., Banday A. J., Górski K. M., Bennett K., Jonas J. L., Tauber J., 2002, *A&A*, 387, 82
- Gold B. et al., 2011, *ApJS*, 192, 15
- Górski K. M., Hivon E., Banday A. J., Wandelt B. D., Hansen F. K., Reinecke M., Bartelmann M., 2005, *ApJ*, 622, 759
- Guzmán A. E., May J., Alvarez H., Maeda K., 2011, *A&A*, 525, A138
- Han J., 2009, in *IAU Symposium*, Vol. 259, *IAU Symposium*, Strassmeier K. G., Kosovichev A. G., Beckman J. E., eds., pp. 455–466
- Haslam C. G. T., Salter C. J., Stoffel H., Wilson W. E., 1982, *A&AS*, 47, 1
- Heiles C., 1974, *A&AS*, 14, 557
- Heiles C., 1984, *ApJS*, 55, 585
- Heiles C., 1998, in *Lecture Notes in Physics*, Berlin Springer Verlag, Vol. 506, *IAU Colloq. 166: The Local Bubble and Beyond*, Breitschwerdt D., Freyberg M. J., Truemper J., eds., pp. 229–238
- Heiles C., 2000, *AJ*, 119, 923
- Heiles C., Chu Y.-H., Troland T. H., Reynolds R. J., Yegingil I., 1980, *ApJ*, 242, 533
- Hinshaw G. et al., 2013, *ApJS*, 208, 19
- Jaffe T. R., Leahy J. P., Banday A. J., Leach S. M., Lowe S. R., Wilkinson A., 2010, *MNRAS*, 401, 1013
- Jarosz N. et al., 2011, *ApJS*, 192, 14
- Jones D. I., Crocker R. M., Reich W., Ott J., Aharonian F. A., 2012, *ApJ*, 747, L12
- Kalberla P. M. W., Burton W. B., Hartmann D., Arnal E. M., Bajaja E., Morras R., Pöppel W. G. L., 2005, *A&A*, 440, 775
- Katayama N., Komatsu E., 2011, *ApJ*, 737, 78
- Koo B.-C., Heiles C., Reach W. T., 1992, *ApJ*, 390, 108
- Lallement R., Welsh B. Y., Vergely J. L., Crifo F., Sfeir D., 2003, *A&A*, 411, 447
- Landecker T. L., Routledge D., Reynolds S. P., Smegal R. J., Borkowski K. J., Seward F. D., 1999, *ApJ*, 527, 866
- Large M. I., Quigley M. F. S., Haslam C. G. T., 1966, *MNRAS*, 131, 335
- Large M. I., Quigley M. J. S., Haslam C. G. T., 1962, *MNRAS*, 124, 405
- Lawson K. D., Mayer C. J., Osborne J. L., Parkinson M. L., 1987, *MNRAS*, 225, 307
- Lewis A., Challinor A., Lasenby A., 2000, *ApJ*, 538, 473
- Liu H., Mertsch P., Sarkar S., 2014, *ApJ*, 789, L29
- López-Caniego M., Massardi M., González-Nuevo J., Lanz L., Herranz D., De Zotti G., Sanz J. L., Argüeso F., 2009, *ApJ*, 705, 868
- Macellari N., Pierpaoli E., Dickinson C., Vaillancourt J. E., 2011, *MNRAS*, 418, 888
- Mao S. A. et al., 2012, *ApJ*, 755, 21
- Mathewson D. S., Ford V. L., 1970, *AJ*, 75, 778
- Mertsch P., Sarkar S., 2013, *Journal of Cosmology and Astroparticle Physics*, 6, 41
- Milogradov-Turin J., Urošević D., 1997, *Bulletin Astronomique de Belgrade*, 155, 41
- Miville-Deschênes M.-A., Ysard N., Lavabre A., Ponthieu N., Macías-Pérez J. F., Aumont J., Bernard J. P., 2008, *A&A*, 490, 1093
- Mortonson M. J., Seljak U., 2014, *ArXiv e-prints*
- Oppermann N. et al., 2012, *A&A*, 542, A93
- Page L. et al., 2007, *ApJS*, 170, 335
- Planck Collaboration et al., 2013, *A&A*, 554, A139
- Platania P., Burigana C., Maino D., Caserini E., Bersanelli M., Cappellini B., Mennella A., 2003, *A&A*, 410, 847
- Preibisch T., Mamajek E., 2008, *The Nearest OB Association: Scorpius-Centaurus (Sco OB2)*, Reipurth B., ed., p. 235
- Puspitarini L., Lallement R., 2012, *A&A*, 545, A21
- Quigley M. J. S., Haslam C. G. T., 1965, *Nature*, 208, 741
- Quinn J. L., 2012, *A&A*, 538, A65
- Reich P., Reich W., 1988, *A&AS*, 74, 7
- Reynolds S. P., Gaensler B. M., Bocchino F., 2012, *Space Sci.Rev.*, 166, 231
- Rubiño-Martín J. A., López-Caraballo C. H., Génova-Santos R., Rebolo R., 2012, *Advances in Astronomy*, 2012
- Serkowski K., 1958, *Acta. Astron.*, 8, 135
- Simmons J. F. L., Stewart B. G., 1985, *A&A*, 142, 100
- Sofue Y., 1977, *A&A*, 60, 327
- Sofue Y., 1988, *PASJ*, 40, 567
- Sofue Y., Hamajima K., Fujimoto M., 1974, *PASJ*, 26, 399
- Sofue Y., Reich W., Reich P., 1989, *ApJ*, 341, L47
- Spoelstra T. A. T., 1971, *A&A*, 13, 237
- Spoelstra T. A. T., 1972, *A&A*, 21, 61
- Spoelstra T. A. T., 1973, *A&A*, 24, 149
- Strong A. W., Moskalenko I. V., Ptuskin V. S., 2007, *Annual Review of Nuclear and Particle Science*, 57, 285
- Strong A. W., Moskalenko I. V., Reimer O., 2004, *ApJ*, 613, 962
- Strong A. W., Orlando E., Jaffe T. R., 2011, *A&A*, 534, A54
- Taylor A. R., Stil J. M., Sunstrum C., 2009, *ApJ*, 702, 1230
- Tomisaka K., 1992, *PASJ*, 44, 177
- Vaillancourt J. E., 2006, *PASP*, 118, 1340

- van der Laan H., 1962, MNRAS, 124, 125
Vidal M., Leahy J. P., Dickinson C., 2014, ArXiv e-prints
Wardle J. F. C., Kronberg P. P., 1974, ApJ, 194, 249
Weaver H., 1979, in IAU Symposium, Vol. 84, The Large-Scale Characteristics of the Galaxy, Burton W. B., ed., pp. 295–298
Weaver R., McCray R., Castor J., Shapiro P., Moore R., 1977, ApJ, 218, 377
Wehus I. K., Fuskeland U., Eriksen H. K., 2013, ApJ, 763, 138
Wolleben M., 2007, ApJ, 664, 349
Wolleben M., Landecker T. L., Reich W., Wielebinski R., 2006, A&A, 448, 411

This paper has been typeset from a $\text{\TeX}/\text{\LaTeX}$ file prepared by the author.